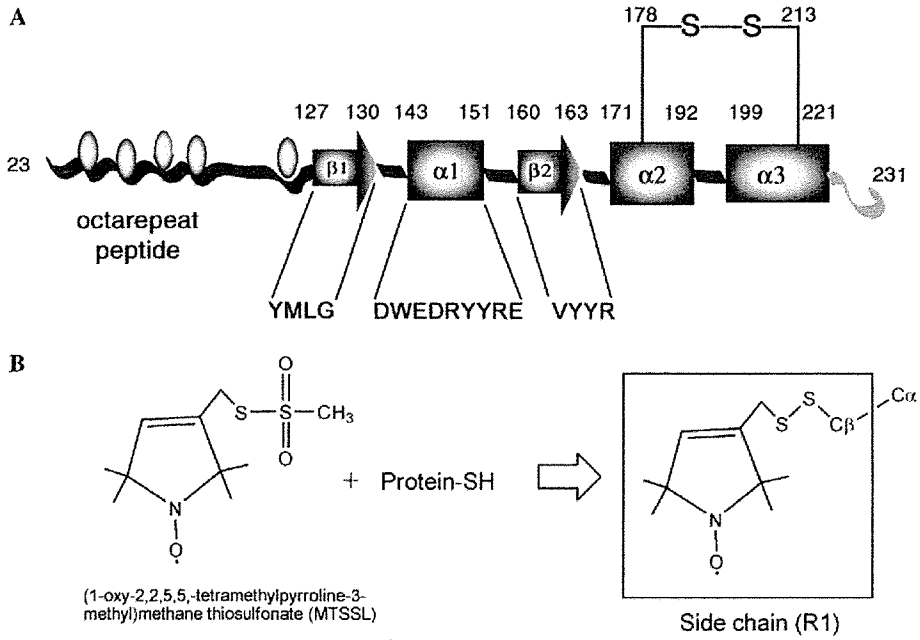


Fig. 1. A schematic diagram of the full-length moPrP and the site-directed spin labeling (SDSL) technique. (A) The full-length moPrP and the target region for SDSL–ESR. The full-length moPrP consisted of 208 amino acids (residues 23–231). The N-terminal domain is largely flexible and has four octapeptide repeats. The C-terminal domain is comprised of three α-helices (H1, H2, and H3) and two β-sheets (S1 and S2). moPrP contains five $Cu^{2+}$-binding sites, two cysteines (codons 178 and 213) forming one disulfide bond, two N-glycosylation sites (codons 180 and 196), and one GPI anchor (C-terminal end). The targets of cysteine mutation are 17 amino acids at H1, S1, and S2. (B) The reaction of the methanethiosulfonate spin-labeling reagent with the cysteine residue generates the nitroxide side chain (R1) on moPrP.

(Helix1, Helix2, and Helix3) and two short anti-parallel β-sheets (Sheet1 and Sheet2) [1,5,6].

Though the precise mechanism of conversion from $PrP^C$ to $PrP^{Sc}$ is still unknown, the accumulation of $PrP^{Sc}$ in endosomes, the main intracellular acidic organelles, indicates that the process of conversion from $PrP^C$ to $PrP^{Sc}$ requires physiological acidic pH conditions [7–9]. Recent circular dichroism (CD) spectroscopic studies showed that acidic conditions in the presence of a denatured agent induce a β-sheet-rich intermediate in human (90–231) and mouse PrP (121–231) *in vitro* [7,10,11]. The study, which used antibodies to probe the structure of recombinant Sylian hamster PrP (residues 90–231), indicated that the conformation of epitopes localized in the C-terminus was insensitive to pH, whereas that of the N-terminus was sensitive [12]. NMR measurement of the full-length human PrP showed that the octapeptide repeats in the N-terminal domain constituted pH-dependent PrP oligomerization; however, this was not detectable around pH-sensitive regions in the C-terminal domain [13]. In contrast, studies using molecular dynamics (MD) simulations proposed the presence of a pH-sensitive region in the C-terminal globular domain on Sylian hamster PrP 109–219, human PrP 125–228, and bovine PrP 124–227 [14,15]. In fact, high resolution NMR and the thermal stability of the globular domain of truncated prion protein (hPrP 121–230) suggested that the residues at the C-terminal end of helix1 and residues 161–164 of β-strand2 were candidates for the "starting point" of pH-induced unfolding and implicated in endosomic $PrP^C$ to $PrP^{Sc}$ conformational transition resulting in TSEs [16]. However, for the full-length $PrP^C$, there is no experimental evidence that low pH induces a conformational change in the globular region of PrP.

Recently, site-directed spin labeling (SDSL) combined with electron spin resonance spectroscopy (ESR) has proven to be a useful technique for protein structural and motional analyses, such as determination of the secondary structure and its orientation, areas of tertiary interactions, and domain mobility [17–20]. The data of SDSL–ESR are applicable for conformational analysis of high molecular weight proteins, whereas NMR and X-ray crystallographic methods are impossible to use for such analysis [17]. In SDSL, the nitroxide side chain (R1) derived from a sulfhydryl-specific nitroxide agent such as a methane thiosulfonate spin label (MTSSL) is introduced into the target codon in the protein sequences by using site-directed mutagenesis (Fig. 1B). Recently, by using this cysteine-scanning spin labeling method to obtain structural information on erythroid α and β spectrin peptides, which are not easily studied by either NMR or X-ray methods, a new amphipathic nature of the helical regions, which is critical in αβ spectrin association at the tetramerization site, was reported by Mehboob et al. [21], indicating that this technique is a powerful tool for monitoring the structure and dynamics of proteins. We have also applied this method to obtain biophysical information on moPrP and reported the thermal stability and pH-dependent mobility changes in three recombinant moPrP mutations (N96C, D143C, and T189C) labeled with MTSSL on the full-length prion protein [22].

In the present study, we used the cysteine-scanning spin-labeling method to analyze the dynamics of recombinant moPrP mutants that were singly labeled at 17 residues in α-helix1 (H1, codon 143–151), β-sheet1 (S1, codon 127–130), and β-sheet2 (S2, codon 160–163). We determined the locations of the pH-sensitive protein sequences in the H1 and S2 regions.

## Materials and methods

*Materials.* (1-Oxy-2,2,5,5-tetramethyl-3-pyrroline-3-methyl) methanethiosulfonate (MTSSL) was purchased from Toronto Research Chemicals (ON, Canada). *Escherichia coli* BL21(DE3)LysS and isopropylthio-β-D-galactoside (IPTG) were from Invitrogen (CA, USA). Ni Sepharose 6 Fast Flow was from Amersham Biosciences Co. (NJ, USA). The TSKgel Phenyl-5PW RP column was from TOSOH (Tokyo, Japan). The Protein Assay Lowry Kit was from Nacalai Tesque, Inc. (Kyoto, Japan). 2-[4-(2-Hydroxyethyl)-L-piperazinyl]ethanesulfonic acid (HEPES) and 2-morpholinoethanesulfonic acid, monohydrate (MES) were from Dojindo, Lab. (Kumamoto, Japan). Other reagents were from Wako Pure Chemical, Co. (Tokyo, Japan).

*Construction of moPrP mutants.* cDNA encoding mouse PrP (residues 23–231) was cloned into *Bam*HI/*Eco*RI sites of pRSETb as described previously [22,23]. In the plasmid encoding moPrP, single amino acids at H1, S1, and S2 were substituted for by cysteine residues (Fig. 1A). These moPrP mutants were generated by the PCR-based site-directed mutagenesis method [22,24]. Oligonucleotides used in the mutagenesis were obtained from Sigma Genosys. The change of the target codons by cysteine residues was confirmed using a CEQ8800 automated sequencer (Beckman Coulter, Inc.).

*Expression and purification of recombinant moPrP mutants.* The expression and purification of recombinant moPrP mutants were modified from those described previously [22]. The expression plasmids were introduced into *E. coli* BL21(DE3)LysS. *E. coli* BL21(DE3)LysS with each moPrP construct was grown overnight in 100 ml SOB liquid culture medium containing 1% sucrose, 0.1 mg/ml ampicillin, and 0.05 mg/ml chloramphenicol at 37 °C. Then 15 ml of overnight culture was added to 450 ml SOB medium with 1% sucrose, 0.1 mg/ml ampicillin, and 0.05 mg/ml chloramphenicol and grown at 37 °C to an optical density at 600 nm of 0.7. Protein expression was induced by adding IPTG to a final concentration at 0.5 mM. The culture was continued for 7 h and then bacterial cells were collected by centrifugation. The bacterial pellets were suspended in 6 M GdnHCl in 20 mM $Na_2HPO_4$ (pH 7.8) and sonicated to completely release the inclusion bodies from BL21(DE3)LysS transformed with expression plasmids. Separated inclusion bodies in 6 M GdnHCl in 20 mM $Na_2HPO_4$ (pH 7.8) were incubated with $Ni^{2+}$-charged chelating Sepharose for 1 h to purify the recombinant moPrP. The protein-bound Sepharose was washed 2× with 8 M urea in 10 mM Tris/HCl and 100 mM $NaH_2PO_4$ (pH 6.2), and then loaded into the column. The recombinant moPrP was eluted using 8 M urea in 10 mM Tris/HCl and 100 mM $NaH_2PO_4$ (pH 4.2). After dialysis against 10 mM acetate buffer (pH 4.0) for 48 h, recombinant moPrP was purified by reverse-phase high performance liquid chromatography (HPLC) using TSKgel Phenyl-5PW RP and a 40–60% linear gradient of acetonitrile with 0.05% trifluoroacetic acid. The purified recombinant moPrP was dialyzed against 10 mM acetate buffer (pH 4.0) for 48 h, concentrated with a centrifugal concentrator (Vivascience) to approximately a quarter of its original volume, and then stored at −80 °C until use. The protein concentration was quantified with the Lowry protein assay using BSA as a standard [25]. The final protein purity (>98%) was confirmed by sodium dodecyl sulfate polyacrylamide gel electrophoresis (SDS–PAGE) and Coomassie brilliant blue staining.

*Spin-labeling of moPrP mutants.* To label the moPrP mutants with MTSSL, a 10-fold molar excess of MTSSL was added to each protein and incubated overnight in the dark at 4 °C. The free MTSSL was removed from the protein using a microdialyzer (Nippon Genetics). To confirm that the α-helix content of spin-labeled moPrP mutants was similar to that of wild-type moPrP, we used a far-UV CD spectropolarimeter (J-820, JASCO) [22]. The sample was diluted to 0.3 mg/ml protein concentration and scanned using a scan speed of 50 nm/min and a response time of 2 s. In all mutants, the two minima (208 and 220 nm), typical of a mainly α-helix-structure protein, were clearly observed and there were no differences in the α-helix content between wild-type moPrP and spin-labeled moPrP mutants [22,26].

*ESR spectroscopy.* Details of the ESR spectroscopy methods have been published elsewhere [22]. The pH change of the sample solution was carried out by dialysis of the sample against the three buffers, 10 mM acetate buffer (pH 5.0), 10 mM MES buffer (pH 6.4), and 10 mM Hepes buffer (pH 7.4). ESR spectra were recorded in a quartz flat cell (RST-DVT05; 50 mm × 4.7 mm × 0.3 mm, Radical Research) for spin-labeled samples of 20 μM moPrP using a JEOL-RE X-band spectrometer (JEOL) with a cylindrical TE011 mode cavity (JEOL). All ESR spectra were obtained at 20 °C, controlled by a temperature controller (ES-DVT4, JEOL), under the following conditions: 5 mW incident microwave power, 100 kHz modulation frequency, 0.2 mT field modulation amplitude, and 10 mT scan range. The $1/\delta H_0$ of the central component ($M_I$=0: $^{14}N$ hyperfine) in the ESR spectrum of spin-labeled $moPrP^C$ was employed as a mobility parameter and was further analyzed using a Win-Rad Radical Analyzer System (Radical Research). To reveal the motional change upon pH variation, we further examined the second moment $\langle H^2 \rangle$, a measure of spectral deviation due to the motional narrowing (or broadening) of ESR spectra. The second moment was estimated numerically with the Win-Rad System.

## Results

### *Mobility change with pH: ESR spectral features from $moPrP^C$*

Fig. 2A shows the ESR spectra from recombinant full-length moPrP mutants in the H1 region at pH 7.4 at 20 °C. Each ESR spectrum from the nine mutants in the H1 region of moPrP showed a different line shape (Fig. 2A). In general, the ESR spectra from H1 region indicate mobile signals with small immobile contributions. The ESR spectra obtained from E145R1 and Y149R1 showed line broadening as compared with those of D143R1 or R150R1, indicating the immobility of the nitroxide probe in E145R1 and Y149R1. To obtain detailed mobility information, we measured the inverse of the peak-to-peak first derivative width of the central resonance ($1/\delta H_0$) in each ESR spectrum in the H1 region, since it has been reported by Hubbell et al. that $1/\delta H_0$ from the ESR spectrum as a mobility parameter is strongly correlated with the local environment of the protein domain structure [17]. The values of $1/\delta H_0$ obtained from the ESR spectra of D143R1, R147R1, R150R1, and E151R1 were approximately 4.07, 2.82, 3.50, and 3.35, respectively. On the other hand, those obtained from the ESR spectra of E145R1 and Y149R1 were approximately 2.19 and 2.75, respectively. The plotted data of $1/\delta H_0$ shown in Fig. 2B indicate the periodical changes in the H1 region. In the S1 region, the ESR spectrum of M129R1 was slightly narrower than those of the other positions in S2 (Fig. 3A) and the $1/\delta H_0$ (3.20) of the M128R1 mutant was slightly higher than those of Y127R1 (2.86), L129R1 (2.88), and G130R1 (2.84) (Fig. 3B). In the S2 region, there were no differences in the line shapes of the ESR spectra of V160R1, Y161R1, Y162R1, and R163R1 (Fig. 4A), and the values of $1/\delta H_0$

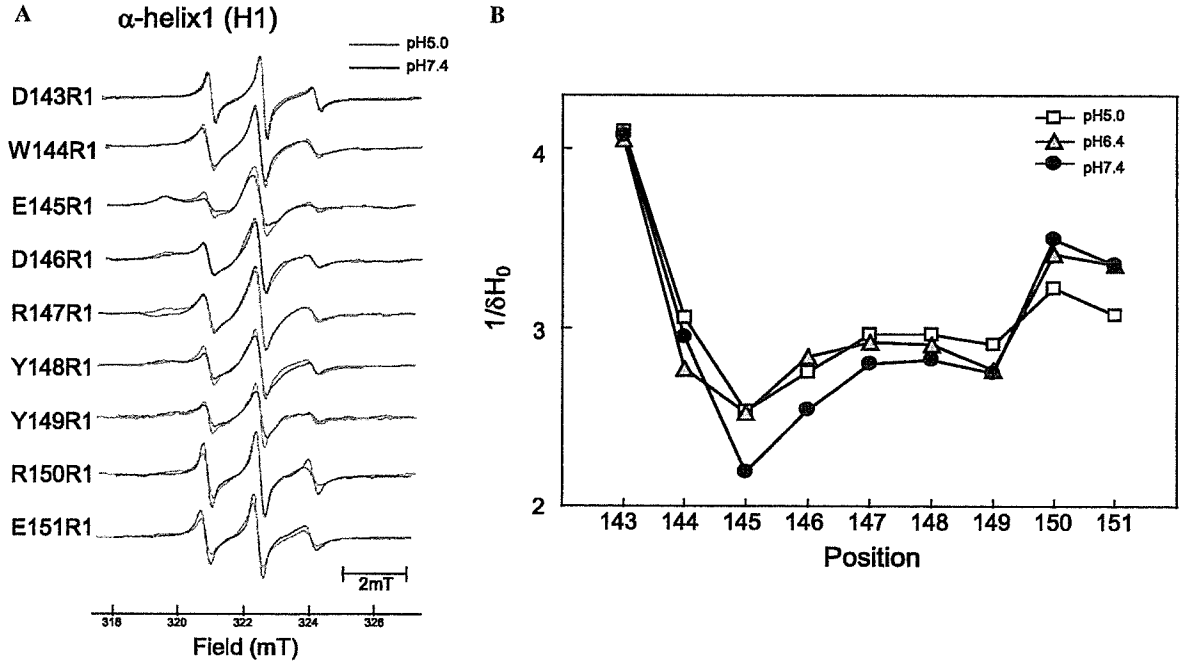


Fig. 2. ESR spectra of α-helix1 (H1) mutants and effects of pH on their line shapes. (A) ESR spectra of nine moPrP mutants at pH 7.4 (black line) and pH 5.0 (red line) were recorded using an X-band ESR spectrometer at 20 °C. (B) The pH-dependent changes in domain mobility of moPrP mutants. The values of $1/\delta H$ obtained from the peak-to-peak central component ($M_I = 0$) in the ESR spectra of spin-labeled moPrP$^C$ at H1 were plotted as a function of pH. (For interpretation of the references to colour in this figure legend, the reader is referred to the web version of this article).

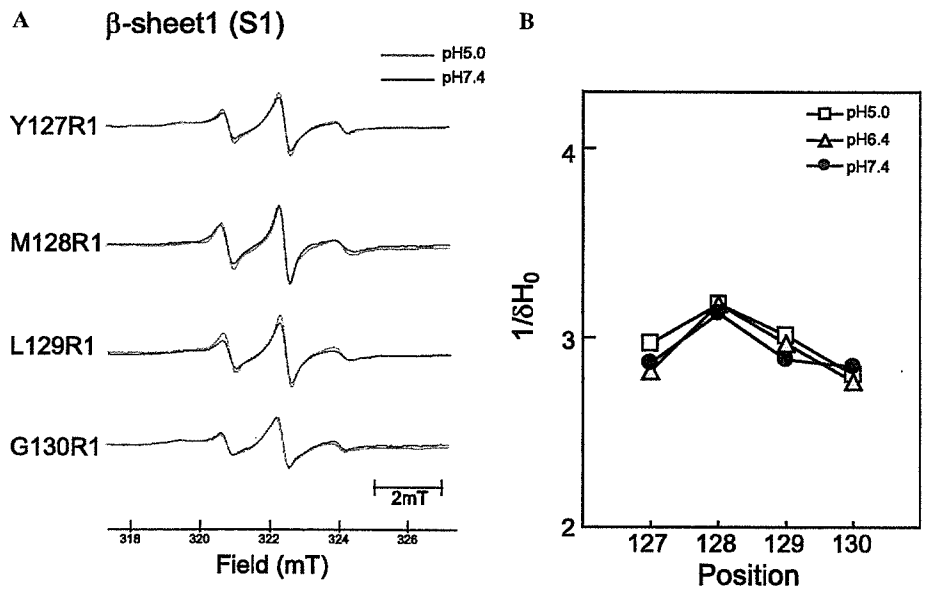


Fig. 3. ESR spectra of β-sheet1 (S1) mutants and effects of pH on their line shapes. (A) ESR spectra of four moPrP mutants were recorded at pH 7.4 (black line) and pH 5.0 (red line) at 20 °C. (B) The values of $1/\delta H_0$ of the nitroxide probes of S1 mutants are plotted as a function of pH. (For interpretation of the references to colour in this figure legend, the reader is referred to the web version of this article).

from the ESR spectra of these four mutants ranged from 2.1 to 2.3, indicating that the nitroxide probes in S2 were strongly immobilized in comparison with those in S1 (Fig. 4B).

*pH-induced conformational changes in moPrP$^C$*

Since it has been suggested that acidic pH is involved in the conformational transition from PrP$^C$ to PrP$^{Sc}$ [7–9], we examined the effects of pH changes on the line shapes of ESR spectra of moPrP$^C$ as shown in Figs. 2A, 3A, and 4A. In the H1 region, each mutant showed a different pattern for the variation of the ESR spectrum during the reduction of pH. When pH in the solution decreased from pH 7.4 to pH 5.0 at 20 °C, there was no significant change in the ESR spectrum of D143R1, but the ESR spectrum of E145R1 became narrow, indicating a pH-dependent

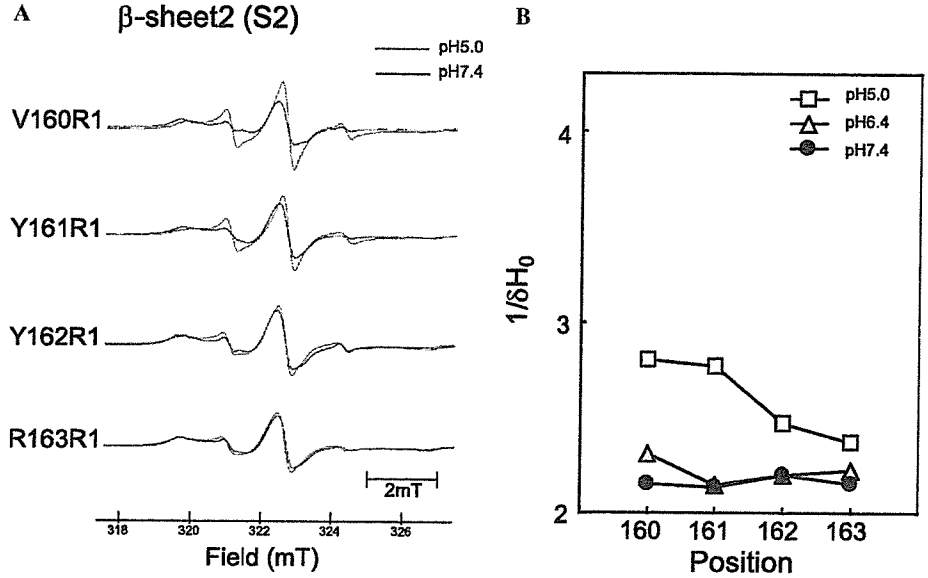


Fig. 4. ESR spectra of β-sheet2 (S2) mutants and effects of pH on their line shapes. (A) ESR spectra of four S2 mutants at 20 °C and pH 7.4 (black line) and pH 5.0 (red line). (B) The values of $1/\delta H_0$ of the nitroxide probes of S2 mutants are plotted as a function of pH. (For interpretation of the references to colour in this figure legend, the reader is referred to the web version of this article).

conformational change from a rigid to a flexible structure. In contrast to this, the decrease of pH-induced line broadening in the ESR spectra of R150R1 and R151R1. In the β-sheet regions, no pH-dependent changes in the line shapes of ESR spectra of S1 were observed (Fig. 3A). However, the decrease of pH-induced narrow line shapes in the ESR spectra of V160R1 and Y161R1 in S2.

Figs. 2B, 3B, and 4B show the pH-dependent changes of $1/\delta H_0$ from ESR spectra in various regions at 20 °C. In the H1 region, the value of $1/\delta H_0$ of D143R1 at pH 5.0 was similar to that of pH 7.4. However the $1/\delta H_0$ of E145R1 increased from 2.2 to 2.5 when the pH in the solution slightly changed from 7.4 to 6.4 and remained constant at the high level of pH 5.0. The values of $1/\delta H_0$ of D146R1 and R147R1 also slightly increased at pH 6.4 in comparison with pH 7.4. In contrast, the values of $1/\delta H_0$ of R150R1 and E151R1 decreased when the pH in the solution decreased from 6.4 to 5.0. On the other hand, the pH-dependent change in $1/\delta H_0$ was not observed in the S1 region. The values of $1/\delta H_0$ of V160R1, Y161R1, Y162R1, and R163R1 in the S2 region increased when pH in the solution decreased from 6.4 to 5.0, but the changes in $1/\delta H_0$ of Y162R1 and R163R1 resulting from a decrease of pH from 6.4 to 5.0 were relatively small.

## Discussion

Structural studies by NMR of recombinant hPrP (23–230) [13,27], moPrP (23–231) [28], and hamster PrP (29–231) [29] revealed a highly flexible N-terminal octapeptide repeat region and C-terminal global region. Figs. 5B and C shows global features of the refined NMR structure of the C-terminal globular region, moPrP (121–231), as reported by Riek et al. [30]. Prion proteins in the cell are attached to the plasma membrane via a glycosyl phosphatidylinositol (GPI) anchor and localized in membrane lipid rafts [1,31]. Lipid rafts, which are rich in spingolipids and cholesterol, are associated with endocytosis. Endosomes and lysosomes are typical acidic organelles [32], their luminal pH is formed by vacuolar type proton ATPase (V-ATPase) and varies between 6.5 and 4.5 [33,34]. Many past studies demonstrated the relationship between the pH of intracellular acidic compartments and conversion from $PrP^C$ to $PrP^{Sc}$ [7–16,35]. Recently, the *in vivo* conversion of human brain $PrP^C$ to a $PrP^{Sc}$-like form was reported to be enhanced at acidic pH [36] and biophysical studies have shown that the free energy of unfolding of hPrP (90–231) is lower at acidic pH than at neutral pH [10]. A β-sheet-rich folding intermediate was observed for moPrP (121–231) at low pH in urea but was also seen at neutral pH [37]. The mechanism for pH-dependent structural changes of prion protein was reported in molecular dynamics (MD) simulation studies [14,15,38]. On the other hand, experimental data about the pH-sensitive region of prion proteins seem to be insufficient although there was one report suggesting that the C-terminal end of Helix1 and 161–164 of S2 have a larger tendency to unfold as revealed by NMR with amide proton protection factor mapping of the globular domain of PrP [16].

The SDSL–ESR technique can be used to analyze high molecular weight proteins for which NMR spectroscopic and X-ray crystallographic methods are not generally applicable [17–20]. In the present study, we employed the SDSL–ESR technique to obtain experimental information on pH-sensitive regions of recombinant $moPrP^C$. Hubbell et al. first used the inverse of peak-to-peak first derivative width of the central resonance ($1/\delta H_0$) of the ESR spectrum as a mobility parameter [17]. We also measured the

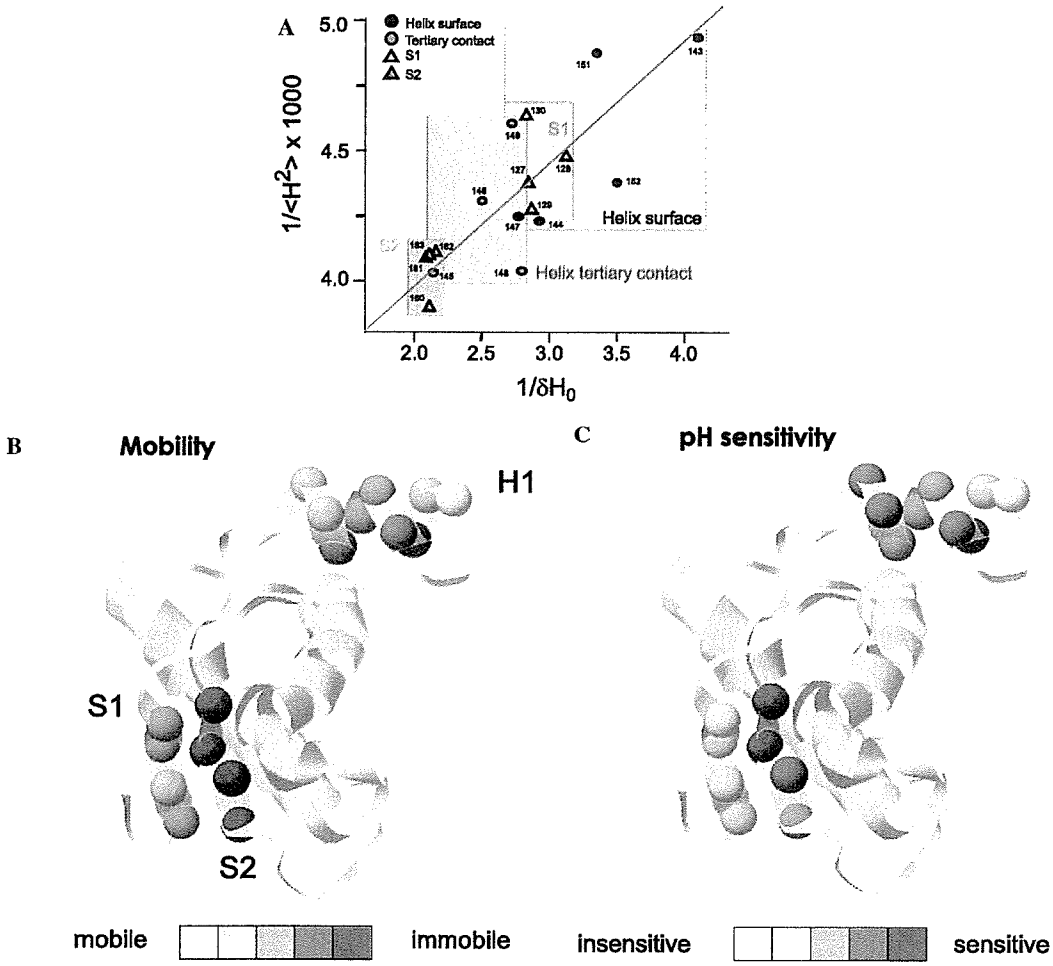


Fig. 5. The dependency of the mobility parameters of the ESR spectrum on the 3D structure of PrP and identification of pH-sensitive regions of PrP. (A) The general relationship between the mobility of the nitroxide side chain and salient features of the moPrP. The inverse spectral second moments ($1/\langle H^2 \rangle$) and the inverse central linewidths ($1/\delta H_0$) for the R1 side chain at 17 sites in moPrP are expressed as semiempirical parameters of mobility. The topographic regions of moPrP were classified into four protein folding categories; i.e., the helix surface site, the helix tertiary contact site, S1 (the surface side), and S2 (the buried side). The light gray line shows the regression linear fitting between these two mobility parameters. The value, $r$=0.80 ($n$=17) of Pearson's correlation coefficient obtained from these two parameters, was greater than the 1% significance value, $r$=0.606 ($n$=17), indicating that the reciprocal central linewidth was positively correlated with the inverse of the spectral second moments. (B) The variation of mobility obtained from ESR spectra of recombinant moPrP mutants in physiological conditions (pH 7.4). Each α-carbon position indicated by graduated colors for relative mobility was superimposed on the 3D structure of moPrP as reported by an NMR study (PDB entry 1AG2, [28]). (C) The 3D positions of pH-sensitive regions of PrP. The magnitude of mobility change induced by a decrease from pH 7.4 to pH 5.0 was qualitatively evaluated. Each α-carbon indicated by graduated colors for relative pH sensitivity was superimposed on the 3D structure of moPrP as reported by an NMR study [28]. (For interpretation of the references to colour in this figure legend, the reader is referred to the web version of this article).

$1/\delta H_0$ in ESR spectra at pH 7.4 and 20 °C. Figs. 2B, 3B, and 4B show the values of $1/\delta H_0$ obtained from the cysteine-scanning SDSL–ESR data of H1, S1, and S2, respectively. In the H1 region, a periodical change of $1/\delta H_0$ was observed. In comparison with the 3D structure of moPrP as estimated by NMR data, shown in Fig. 5B, highly mobile residues of the nitroxide probe in D143R1, R147R1, and R150R1 were located on the outer surface of H1, whereas low mobility residues such as E145R1 and Y149R1 were in the inner contact residues of H1. These variations of mobility in the nitroxide probe were well correlated with the 3D helix structure of moPrP. On the other hand, the fluctuation in the values of $1/\delta H_0$ of the S1 region in neutral pH solution of moPrP was small, although the value at M128R1 was observed to be relatively high (Fig. 3B). Furthermore, the values of $1/\delta H_0$ of the S2 region were lower than those of the S1 region (Figs. 3B and 4B). The 3D structure of moPrP identified by NMR (Fig. 5B) showed that the S2 region was located in the buried structure close to H2 and H3, whereas the S1 region was located in the relatively outer side of moPrP. The difference of mobility between S1 and S2 regions can probably be explained by the difference of the tertiary structure of moPrP. To define the relationship between structure and mobility, with the aid of $1/\delta H_0$, it is convenient to employ a further semiempirical parameter for mobility reflected in ESR spectra: namely the spectral breadth, which is represented by the spectral second moment

($<H^2>$) [39]. The numerical values of these quantities are mainly determined by the degree of averaging of magnetic tensor values. As the frequency of nitroxide rotational motion is lowered, the second moment and the line width increase. Fig. 5A shows a plot of the reciprocal second moment ($1/<H^2>$) versus the reciprocal central line width ($1/\delta H_0$) for the spectra of R1 side chains representing the helix surface, helix tertiary contact, and two β-sheets (S1 and S2). As shown in Fig. 5A, the mobility was consistent with the tertiary fold of moPrP and there was a linear correlation between these two parameters. These results indicated that these parameters were related to the 3D structure of PrP.

Since recent reports [7–16,35] showed that exposure of prion proteins to low pH in endosomes was essential for the conversion from $PrP^C$ to $PrP^{Sc}$, we tried to identify pH-sensitive regions by using the cysteine-scanning spin-labeling technique as described above. In the H1 region, we observed increases of $1/\delta H_0$ at E145R1, D146R1, and R147R1 when pH was decreased from 7.4 to 6.4 (Fig. 2). The values of R150R1 and E151R1 at pH 6.4 were similar to those at pH 7.4, but these values suddenly dropped when the pH in the solution changed from pH 6.4 to pH 5.0 as shown in Fig. 2B. In β-sheet regions of PrP, as shown in Fig. 3B, the mobility of S1 was conserved against a decrease of pH. However, the values of $1/\delta H_0$ at all four residues of S2 increased when pH was decreased from 6.4 to 5.0 (Fig. 4B). In particular, the region containing two N-terminal residues of S2, V160R1, and Y161R1 was identified as a more pH-sensitive region than that of C-terminal side residues of S2. Thus, the pH-sensitive domains, including the N-terminal tertiary contact site of H1 and the C-terminal ends of H1 and S2 regions, were identified in recombinant moPrP as shown in Fig. 5C. It is noteworthy that a slight decrease from pH 7.4 to 6.4 induced conformational changes in the N-terminal tertiary contact residues of H1 (E145R1, D146R1, and R147R1) though conformational changes in the C-terminal end of H1 (R150R1 and E151R1) and N-terminal residues of S2 (V160R1 and Y161R1) required a large change from pH 7.4 to 5.0. These findings led us to speculate that the conformational change from the tertiary contact structure to a more flexible structure in N-terminal residues of H1 was the first step for unfolding of PrP, followed by secondary conformational changes of S2 and the C-terminal end of H1.

In a previous NMR study of the globular domain (121–231) of hPrP [16], two domains, the C-terminal ends of the H1 and S2 regions, were identified as the pH-sensitive regions for acid-induced unfolding leading to a β-sheet rich structure. In addition to these two sites, the present SDSL–ESR study clearly demonstrated that the N-terminal region (E145, D146, and R147) of H1 was also a pH-sensitive region. The N-terminal tertiary contact region of H1 may be important for conversion from $PrP^C$ to $PrP^{Sc}$ in acidic conditions, since the structural change in this region easily occurred in a mildly acidic condition (pH 6.4) in comparison with the other two pH-sensitive regions. According to recent studies using MD simulations for PrP, histidine at 186 and asparagic acid at 177 of PrP were reported to be candidates for the amino acid residues that trigger the conversion to β-sheet-rich PrP [38,40]. This conversion model was based on the 3D structural changes due to disruption of a salt bridge with protonation of their amino acid residues caused by a decrease of pH. It is unclear whether these amino-acid residues were actually associated with pH-dependent conformational changes in H1 and S2 as observed in the present study. Further experiments to clarify this are now in progress.

In summary, the present cysteine-scanning SDSL–ESR study for H1, S1, and S2 of moPrP provided experimental evidence for three pH-sensitive sites, (1) the N-terminal tertiary contact site of H1, (2) the C-terminal end of H1, and (3) the S2 region. In particular, the present identification is the first report on a conformational change in the N-terminal tertiary contact site of H1 induced by mildly acidic conditions. This conformational change may be the first step in conversion of $PrP^C$ to the pathogenic $PrP^{Sc}$ structure in intracellular acidic organelles.

## Acknowledgments

This work was supported, in part, by Grants-in-Aid for Basic Scientific Research from the Ministry of Education, Culture, Sports, Science and Technology of Japan (No. 17380178 and No. 18658118 [O.I.] and No. 17580275 and No. 17658126 [M.K.]), by Research Grants from the Program for the Center of Excellence of Zoonosis Control, Sapporo 060-0818, Japan [Y.W., O.I., M.H.], and CREST-JST, Multi-Quantum Coherence ESR Project, Muroran 050-8585, Japan [Y.S.].

## References

[1] S.B. Prusiner, Prions, Proc. Natl. Acad. Sci. USA 95 (1998) 13363–13383.
[2] C. Weissmann, The Ninth Datta Lecture. Molecular biology of transmissible spongi form encephalopathies, FEBS Lett. 389 (1996) 3–11.
[3] S.B. Prusiner, Molecular biology of prion diseases, Science 252 (1991) 1515–1522.
[4] J.S. Griffith, Self-replication and scrapie, Nature 215 (1967) 1043–1044.
[5] C. Weissmann, Molecular genetics of transmissible spongiform encephalopathies, J. Biol. Chem. 274 (1999) 3–6.
[6] A. Aguzzi, M. Glatzel, F. Montrasio, M. Prinz, F.L. Heppner, Interventional strategies against prion diseases, Nat. Rev. Neurosci. 2 (2001) 745–749.
[7] S. Hornemann, R. Glockshuber, A scrapie-like unfolding intermediate of the prion protein domain PrP (121–231) induced by acidic pH, Proc. Natl. Acad. Sci. USA 95 (1998) 6010–6014.
[8] J.W. Kelly, The environmental dependency of protein folding best explains prion and amyloid diseases, Proc. Natl. Acad. Sci. USA 95 (1998) 930–932.
[9] W. Swietnicki, M. Morillas, S.G. Chen, P. Gambetti, W.K. Surewicz, Aggregation and fibrillization of the recombinant human prion protein huPrP (90—231), Biochemistry 39 (2000) 424–431.

[10] W. Swietnicki, R. Petersen, P. Gambetti, W.K. Surewicz, pH-dependent stability and conformation of the recombinant human prion protein PrP(90-231), J. Biol. Chem. 272 (1997) 27517–27520.
[11] G.S. Jackson, A.F. Hill, C. Joseph, L. Hosszu, A. Power, J.P. Waltho, A.R. Clarke, J. Collinge, Multiple folding pathways for heterologously expressed human prion protein, Biochim. Biophys. Acta. 1431 (1999) 1–13.
[12] Y. Matsunaga, D. Peretz, A. Williamson, D. Burton, I. Mehlhorn, D. Groth, F.E. Cohen, S.B. Prusiner, M.A. Baldwin, Cryptic epitopes in N-terminally truncated prion protein are exposed in the full-length molecule: dependence of conformation on pH, Proteins 44 (2001) 110–118.
[13] R. Zahn, The octapeptide repeats in mammalian prion protein constitute a pH-dependent folding and aggregation site, J. Mol. Biol. 334 (2003) 477–488.
[14] D.O. Alonso, S.J. DeArmond, F.E. Cohen, V. Daggett, Mapping the early steps in the pH-induced conformational conversion of the prion protein, Proc. Natl. Acad. Sci. USA 98 (2001) 2985–2989.
[15] D.O. Alonso, C. An, V. Daggett, Simulations of biomolecules: characterization of the early steps in the pH-induced conformational conversion of the hamster, bovine and human forms of the prion protein, Philos. Transact. A Math. Phys. Eng. Sci. 2002 (2002) 1165–1178.
[16] L. Calzolai, R. Zahn, Influence of pH on NMR structure and stability of the human prion protein globular domain, J. Biol. Chem. 278 (2003) 35592–35596.
[17] W.L. Hubbell, H.S. Mchaourab, C. Altenbach, M.A. Lietzow, Watching proteins move using site-directed spin labeling, Structure 4 (1996) 779–783.
[18] W.L. Hubbell, D.S. Cafiso, C. Altenbach, Identifying conformational changes with site-directed spin labeling, Nat. Struct. Biol. 7 (2000) 735–739.
[19] K.J. Oh, H. Zhan, C. Cui, K. Hideg, R.J. Collier, W.L. Hubbell, Organization of diphtheria toxin T domain in bilayers: a site-directed spin labeling study, Science 273 (1996) 810–812.
[20] L. Columbus, W.L. Hubbell, A new spin on protein dynamics, Trends Biochem. Sci. 27 (2002) 288–295.
[21] S. Mehboob, B.-H. Luo, W. Fu, M.E. Johnson, L.W.-M. Fung, Conformational studies of the tetramerization site of human erythroid spectrin by cysteine-scanning spin-labeling EPR methods, Biochemistry 44 (2005) 15898–15905.
[22] O. Inanami, S. Hashida, D. Iizuka, M. Horiuchi, W. Hiraoka, Y. Shimoyama, H. Nakamura, F. Inagaki, M. Kuwabara, Conformational change in full-length mouse prion: a site-directed spin-labeling study, Biochem. Biophys. Res. Commun. 335 (2005) 785–792.
[23] C.L. Kim, A. Umetani, T. Matsui, N. Ishiguro, M. Shinagawa, M. Horiuchi, Antigenic characterization of an abnormal isoform of prion protein using a new diverse panel of monoclonal antibodies, Virology 320 (2004) 40–51.
[24] Y. Imai, Y. Mastushima, T. Sugimura, M. Terada, A simple and rapid method for generating a deletion by PCR, Nucleic Acid Res. 19 (1991) 2785.
[25] O.H. Lowry, N.J. Rosebrough, A.L. Farr, R.J. Randall, Protein measurement with the Folin phenol reagent, J. Biol. Chem. 193 (1951) 265–275.
[26] N.R. Maiti, W.K. Surewicz, The role of disulfide bridge in the folding and stability of the recombinant human prion protein, J. Biol. Chem. 276 (2001) 2427–2431.
[27] R. Zahn, A. Liu, T. Lührs, R. Riek, C. Schroetter, F.L. García, M. Billeter, L. Calzolai, G. Wider, K. Wüthrich, NMR solution structure of the human prion protein, Proc. Natl. Acad. Sci. USA 97 (2000) 145–150.
[28] S. Hornemann, C. Korth, B. Oesch, R. Rieka, G. Widera, K. Wüthrich, R. Glockshubera, Recombinant full-length murine prion protein, mPrP (23–231): purification and spectroscopic characterization, FEBS Lett. 413 (1997) 277–281.
[29] D.G. Donne, J.H. Viles, D. Groth, I. Mehlhorn, T.L. James, F.E. Cohen, S.B. Prusiner, P.E. Wright, H.J. Dyson, Structure of the recombinant full-length hamster prion protein PrP (29–231): The N terminus is highly flexible, Proc. Natl. Acad. Sci. USA 94 (1997) 13452–13457.
[30] R. Riek, G. Wider, M. Billeter, S. Hornemann, R. Glockshuber, K. Wüthrich, Prion protein NMR structure and familial human spongiform encephalopathies, Proc. Natl. Acad. Sci. USA 95 (1998) 11667–11672.
[31] M. Vey, S. Pilkuhn, H. Wille, R. Nixon, S.J. DeArmond, E.J. Smart, R.G. Anderson, A. Taraboulos, S.B. Prusiner, Subcellular colocalization of the cellular and scrapie prion proteins in caveolae-like membranous domains, Proc. Natl. Acad. Sci. USA 93 (1996) 14945–14949.
[32] R.J. Lee, S. Wang, P.S. Low, Measurement of endosome pH following folate receptor-mediated endocytosis, Biochim. Biophys. Acta 1312 (1996) 237–242.
[33] G.H. Sun-Wada, Y. Wada, M. Futai, Vascuolar $H^+$ pumping ATPase in luminal acidic organelles and extracellular compartments: common rotational mechanism and diverse physiological roles, J. Bioenerg. Biomembr. 35 (2003) 347–358.
[34] G.H. Sun-Wada, Y. Wada, M. Futai, Lysosome and lysosome-related organelles responsible for specialized functions in higher organisms, with special emphasis on vacuolar-type proton ATPase, Cell Struct. Funct. 28 (2003) 455–463.
[35] M.L. DeMarco, V. Daggett, Local environmental effects on the structure of the prion protein, C. R. Biol. 28 (2005) 847–862.
[36] W.-Q. Zou, N.R. Cashman, Acidic pH and detergents enhance *in vitro* conversion of human, brain $PrP^C$ to a $PrP^{Sc}$ -like form, J. Biol. Chem. 277 (2002) 43942–43947.
[37] D.A. Kocisko, S.A. Priola, G.J. Raymond, B. Chesebro, P.T. Lansbury Jr., B. Caughey, Species specificity in the cell-free conversion of prion protein to protease-resistant forms: a model for the scrapie species barrier, Proc. Natl. Acad. Sci. USA 92 (1995) 3923–3927.
[38] E. Langella, R. Improta, V. Barone, Checking the pH-induced conformational transition of prion protein by molecular dynamics simulations: effect of protonation of histidine residues, Biophys. J. 87 (2004) 3623–3632.
[39] G.E. Pake, T.L. Estle, The Physical Principles of Electron Paramagnetic Resonance, second ed., Benjamin Inc., Reading, 1973 (Chapt. 6).
[40] J. Gsponer, P. Ferrara, A. Caflisch, Flexibility of the murine prion protein and its Asp178Asn mutant investigated by molecular dynamics simulations, J. Mol. Graph. Model 20 (2001) 169–182.

American Journal of Pathology, Vol. 168, No. 3, March 2006

DOI: 10.2353/ajpath.2006.050314

*Immunopathology and Infectious Diseases*

# Pathogenic Role of B Cells in Anti-CD40-Induced Necroinflammatory Liver Disease

Kiminori Kimura,*†‡ Hisataka Moriwaki,* Masahito Nagaki,* Masanao Saio,§ Yasunari Nakamoto,¶ Makoto Naito,‖ Kazuo Kuwata,‡ and Francis V. Chisari†

*From the First Department of Internal Medicine,* Gifu University School of Medicine, Gifu, Japan; the Department of Molecular and Experimental Medicine,† The Scripps Research Institute, La Jolla, California; the Center for Emerging Infectious Diseases,‡ Gifu University, Gifu, Japan; the Department of Immunopathology,§ Gifu University Graduate School of Medicine, Gifu, Japan; the Department of Gastroenterology,¶ Kanazawa University Graduate School of Medicine, Kanazawa, Japan; the Department of Cellular Function,‖ Division of Cellular and Molecular Pathology, Niigata University Graduate School of Medical and Dental Sciences, Niigata, Japan*

**Activated B cells function in antibody production and antigen presentation, but whether they perform any pathophysiological functions at sites of inflammation is not fully understood. Here, we report that intravenous injection of an agonistic anti-CD40 monoclonal antibody (αCD40) causes a biphasic inflammatory liver disease in inbred mice. The late phase of disease was suppressed in B-cell-deficient mice and by the depletion of macrophages, but not T cells or natural killer cells. We also report that SCID mice were not susceptible to αCD40-induced liver disease unless they were reconstituted with normal B cells and that B cells as well as macrophages played key roles in αCD40-induced late phase of liver inflammation. Finally, liver disease and the recruitment of inflammatory cells into the liver were mediated by interferon-γ and tumor necrosis factor-α, but not by Fas. In conclusion, these results indicate that CD40 ligation can trigger a B-cell-mediated inflammatory response that can have pathogenic consequences for the liver.** *(Am J Pathol 2006, 168:786–795; DOI: 10.2353/ajpath.2006.050314)*

B cells produce antibodies that prevent the spread of infections and perform additional effector functions including opsonization, and complement fixation.[1] B cells also function as antigen-presenting cells and can secrete inflammatory cytokines and chemokines under various conditions.[2] Recently, B-cell subsets (termed B effector 1 and 2 cells) that possess distinct cytokine production profiles have been identified.[3] These activities suggest that B cells may be able to regulate the inflammatory response and attract other inflammatory cells to sites of infection. Indeed, it has been demonstrated that B cells participate in the induction of rheumatoid arthritis[4,5] and contribute to experimental autoimmune encephalomyelitis.[6] Moreover, centrilobular and portal B-cell infiltrates occur both in autoimmune hepatitis and chronic viral hepatitis C,[7,8] implying that B cells may also contribute to the pathogenesis of liver injury in those diseases. The latter hypothesis has not been tested, however, because a suitable animal model has not been available.

CD40 is a 50-kd glycoprotein that is present on the surface of B cells, follicular dendritic cells, monocytes, and some endothelial, epithelial, and cancer cells.[9–11] CD40 plays a crucial role in B-cell proliferation; immunoglobulin secretion and differentiation;[11] T-cell activation;[10] and monocyte, macrophage, and dendritic cell functions, including their survival and ability to secrete several inflammatory cytokines.[9,12] Recent studies have shown that anti-CD40 (αCD40) therapy may have a place in the treatment of infectious diseases and cancer. For example, αCD40 induced marked isotype switching and protective antibody responses to a polysaccharide antigen,[13] and indirectly activated natural killer (NK) cells resulting in significant anti-tumor and anti-metastatic effects.[14] Furthermore, CD40 ligation has been shown to trigger an inflammatory response in the lungs secondary to activation of bone marrow-derived CD40-positive cells.[15,16] Finally, CD40 ligation has been shown to induce the secretion of antiviral cytokines that inhibit hepatitis B virus replication in the liver of HBV transgenic mice.[17]

We recently showed that CD40 ligation induces a biphasic inflammatory disease in the mouse liver that

Accepted for publication October 28, 2005.

Supplemental material for this article can be found on *http://ajp.amjpathol.org*.

Address reprint requests to Kiminori Kimura, M.D., Ph.D., Center for Emerging Infectious Diseases, Gifu University, Gifu-shi, Gifu 501-1194, Japan. E-mail: kkimura@cc.gifu-u.ac.jp.

peaks on day 1 and again on day 5,[17] and that nuclear factor (NF)-κB signaling controls this liver inflammation.[18] In the former study, we focused on the mechanisms responsible for the early (day 1) phase of the disease, and demonstrated that it was mainly triggered by activated APCs and mediated by interferon (IFN)-γ and tumor necrosis factor (TNF)-α.[17] In the current study, we focused on the mechanisms responsible for the late (day 5) phase of the disease, and discovered a hitherto unexpected role for activated B cells in the pathogenesis of liver injury, although once again the disease is mediated by IFN-γ and the cells it recruits. Our results indicate that the late phase of inflammatory liver disease induced by CD40 ligation is a macrophage- and B-cell-dependent process, and provide new insight into the pathogenic roles of B cells as effectors of the immune response.

## Materials and Methods

### Mice

$CB6F_1/J$ and C57BL/6 mice were purchased from Japan SLC (Shizuoka, Japan). SCID and C.B.17 mice were obtained from Japan Clea (Shizuoka, Japan). μMT mice were obtained from Jackson Laboratory (Bar Harbor, ME). Fas KO mice[19] were generously provided by Dr. S. Nagata (Osaka University, Osaka, Japan). All animals were housed in pathogen-free rooms under strict barrier conditions, and received humane care according to the guidelines of the Animal Care Committee of Gifu University School of Medicine.

### Anti-CD40 and Anti-Cytokine Antibodies

The FGK45 hybridoma producing a rat IgG2a monoclonal antibody (mAb) against mouse CD40 (αCD40) was kindly provided by Dr. A. Rolink (Basel Institute for Immunology, Basel, Switzerland). Mice were injected intravenously with either 100 μg of αCD40 or 100 μg of purified rat IgG2a (BD Pharmingen, San Diego, CA) as a control. To neutralize IFN-γ and TNF-α, mice were injected intraperitoneally (250 μg/mouse) on days 0 and +2 with 1) hamster mAb H22 specific for murine IFN-γ[20]; 2) hamster mAb TN3 19.12 specific for murine TNF-α[21] (both generously provided by Dr. R. Schreiber, Washington University, St. Louis, MO); or 3) control hamster IgG (Jackson ImmunoResearch, West Grove, PA).

### Enzyme-Linked Immunosorbent Assay

Serum IFN-γ and TNF-α concentrations were assayed using enzyme-linked immunosorbent assay kits (Genzyme Techne Co., Minneapolis, MN) according to the manufacturer's protocols.

### In Vivo *Depletion of $CD4^+$ and $CD8^+$ T Cells, NK Cells, and Macrophages*

To deplete $CD4^+$ and $CD8^+$ T cells, mice were injected intravenously with rat anti-mouse CD4 (YTS191.1) and rat anti-mouse CD8 (YTS169.4) mAb,[22] both kindly provided by Dr. R. Zinkernagel (University of Zurich, Zurich, Switzerland). To deplete NK cells in the liver, mice were injected intravenously with rabbit anti-mouse asialo-GM1 antibody (50 μg/mouse) (Wako Pure Chemical, Osaka, Japan) on days −1 and +2 relative to the αCD40 injection. Purified rabbit IgG (Sigma-Aldrich, St. Louis, MO) was used as a negative control. To deplete macrophages in the liver, mice were injected intravenously (100 μl/mouse) with liposome-encapsulated dichloromethylene diphosphonate (L-MDP)[23] on days −1 and +2 relative to the αCD40 injection, kindly provided by Dr. M. Naito (Niigata University School of Medicine, Niigata, Japan).

### Tissue DNA and RNA Analyses

Frozen liver was mechanically pulverized under liquid nitrogen and total RNAs were isolated for RNase protection assays (RPA) as previously described.[17] All reagents for RPA were purchased from BD Pharmingen. Specific signals were detected using a BAS-2500 imaging analyzer (Fuji Film, Nakanuma, Japan) and a FLA-3000 phosphoimager (Fuji Film). The mRNA expression levels were calculated as relative percentage values of the L32 housekeeping gene expression by using Image J soft ware.

### Biochemical and Histological Analyses

The extent of hepatocellular injury was monitored biochemically by measuring the serum alanine aminotransferase (sALT) activity at multiple time points using a standard clinical automatic analyzer. For histological analysis, liver tissue was fixed in 10% zinc-buffered formalin, embedded in paraffin, sectioned (3 μm), and stained with hematoxylin and eosin (H&E).

### Immunohistochemistry

For immunofluorescent microscopic analyses, liver sections were fixed with acetone at 4°C for 10 minutes, and preincubated with 10 μg/ml of rat anti-CD16/32 antibody (clone 2.4G2, BD Pharmingen) for 30 minutes. The sections were then incubated with rat anti-mouse B220-PE (clone RA3-6B2, BD Pharmingen) followed by rat anti-mouse IgM-FITC (clone R6-60.2, BD Pharmingen) for 1 hour each at room temperature. After each step of the staining, the sections were washed three times with phosphate-buffered saline (PBS) for 10 minutes each. Finally, the sections were observed using a DMRA fluorescence microscope and the QFISH software (Leica Microsystems Imaging Solutions, Cambridge, UK).

Liver tissues were treated with biotin conjugated with rat anti-mouse B220 mAb (BD Pharmingen) followed by streptavidin biotin-horseradish peroxidase complex (DAKO, Glostrup, Denmark). The reaction was visualized with 0.035% $H_2O_2$ and 0.03% 3,3′-diaminobenzidine (WAKO, Tokyo, Japan) in 50 mmol/L Tris-HCl (pH 7.6) for 2 to 3 minutes. After 4% formaldehyde fixation,

specimens were counterstained with hematoxylin and observed.

### *IHLs*

To isolate intrahepatic leukocytes (IHLs), single-cell suspensions were prepared from liver perfused with PBS via the inferior vena cava and were digested in 10 ml of RPMI 1640 (Life Technologies, Gaithersburg, MD) containing 0.02% (w/v) collagenase IV (Sigma-Aldrich) and 0.002% (w/v) DNase I (Sigma-Aldrich) for 40 minutes at 37°C. Cells were overlaid on 24% (w/v) metrizamide (Sigma-Aldrich) in PBS. After centrifugation for 20 minutes at 1500 × *g*, IHLs were isolated at the interface.

### *Fluorescence-Activated Cell Sorting (FACS) Analysis*

To examine cytokine production in IHLs, isolated IHLs were cultured *ex vivo* for 4 hours in Brefeldin A (BD Pharmingen) and then stained with anti-CD3, anti-NK1.1, anti-CD11b, anti-CD11c, or anti-B220 (all from BD Pharmingen). After fixation, the cells were permeabilized for 30 minutes in 25 $\mu$l of PBS plus 0.5% saponin. Anti-mouse IFN-$\gamma$, TNF-$\alpha$-PE, or allophycocyanin (APC) or isotype control mAb were added at a final dilution of 1/100, and the cells were incubated for 30 minutes at room temperature. The cells were washed and re-suspended in 1 ml of FACS buffer for analysis using a FACScalibur flow cytometer (BD Immunocytometry Systems, San Jose, CA).

### *Isolation of B Cells*

B cells were purified by negative selection using a B-cell isolation kit (Miltenyi Biotec, Bergisch Gladbach, Germany) according to the manufacturer's instructions. The purified cells were routinely >95% B220$^+$.

### *Data Analysis*

All values in the figures and text are expressed as the mean ± SD. The significance of differences among mean values was evaluated according to the Mann-Whitney *U*-test.

## *Results*

### *A Single Injection of αCD40 Causes a Biphasic Inflammatory Liver Disease*

To determine whether αCD40 causes liver injury in inbred mice, four groups of age- and sex-matched CB6F1 mice (three mice/group) received an intravenous injection of αCD40 (100 $\mu$g/mouse) or rat IgG2a (rat IgG). As shown in Figure 1, sALT activity was mildly elevated (160 ± 32 U/L) at day 1, returned to normal (44 ± 12 U/L) at day 3, and then rebounded (242 ± 36 U/L) at day 5 after the injection.

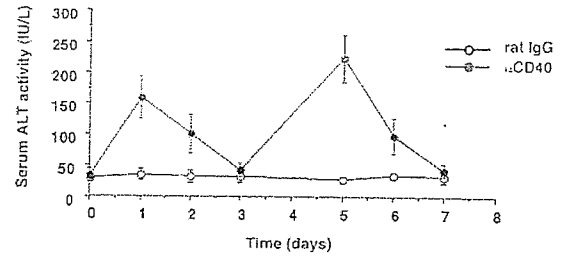


**Figure 1.** Serum ALT activity. CB6F1 mice were injected intravenously with 100 $\mu$g of αCD40 or 100 $\mu$g of rat IgG as a control, and sacrificed at the indicated time points. The mean sALT activity measured at the time of autopsy is indicated for each group and expressed in IU/L.

### *CD40 Ligation Induces Inflammatory Liver Disease*

To evaluate inflammatory cytokine and chemokine expressions in the liver after CD40 ligation, RPA analysis of total liver RNA revealed that αCD40 injection induced CD3, CD4, and CD8 mRNA expression in the liver on day 1, and progressively increased on days 3 and 5 (Figure 2A). These changes were accompanied by clear biphasic increases in IFN-$\gamma$ and TNF-$\alpha$ levels in the serum (Figure 2B) and hepatic interleukin (IL)-1, IL-12, CXCL10, CCL2, CCL4, and CCL5 expression (Figure 2A) on days 1 and 5, reflecting the biphasic increase in sALT activity described above (Figure 1), although the hepatic IFN-$\gamma$ mRNA levels were too low to have confidence in their kinetics. Further, we found that other inflammatory cytokines, Th2 type cytokines, IL-4, IL-5, and IL-6 mRNA expressions were increased faintly on day 5 although IL-10 mRNA expression was gradually elevated until day 5. We also found that the expression of F4/80 mRNA (a macrophage marker[24] that is down-regulated on activation[24–26]) was reduced on days 1 and 5 compared with the rat IgG control mice, suggesting that intrahepatic macrophages were also activated by αCD40 at these time points.[25,26] To determine which cell population produced IFN-$\gamma$ and TNF-$\alpha$ on day 5 after the αCD40 injection, we stained intrahepatic macrophages (CD11b$^+$), dendritic cells (CD11c$^+$), NK cells (NK1.1$^+$), T cells (CD3$^+$), and B cells (B220$^+$) with antibodies against IFN-$\gamma$ and TNF-$\alpha$. As shown in Figure 2C, macrophages and dendritic cells were found to produce TNF-$\alpha$, in contrast, IFN-$\gamma$ was produced by NK cells and at lower levels by T and B cells. We also found that intrahepatic inflammatory cells, including macrophages, dendritic cells, and B cells were detected in the liver, indicating that CD40 ligation induced migration and proliferation of these cells (data not shown).

### *Depletion Experiments*

To determine the role of T cells in the late (day 5) phase of αCD40-induced liver injury, mice were treated with αCD4 and αCD8 mAb or control rat IgG before the

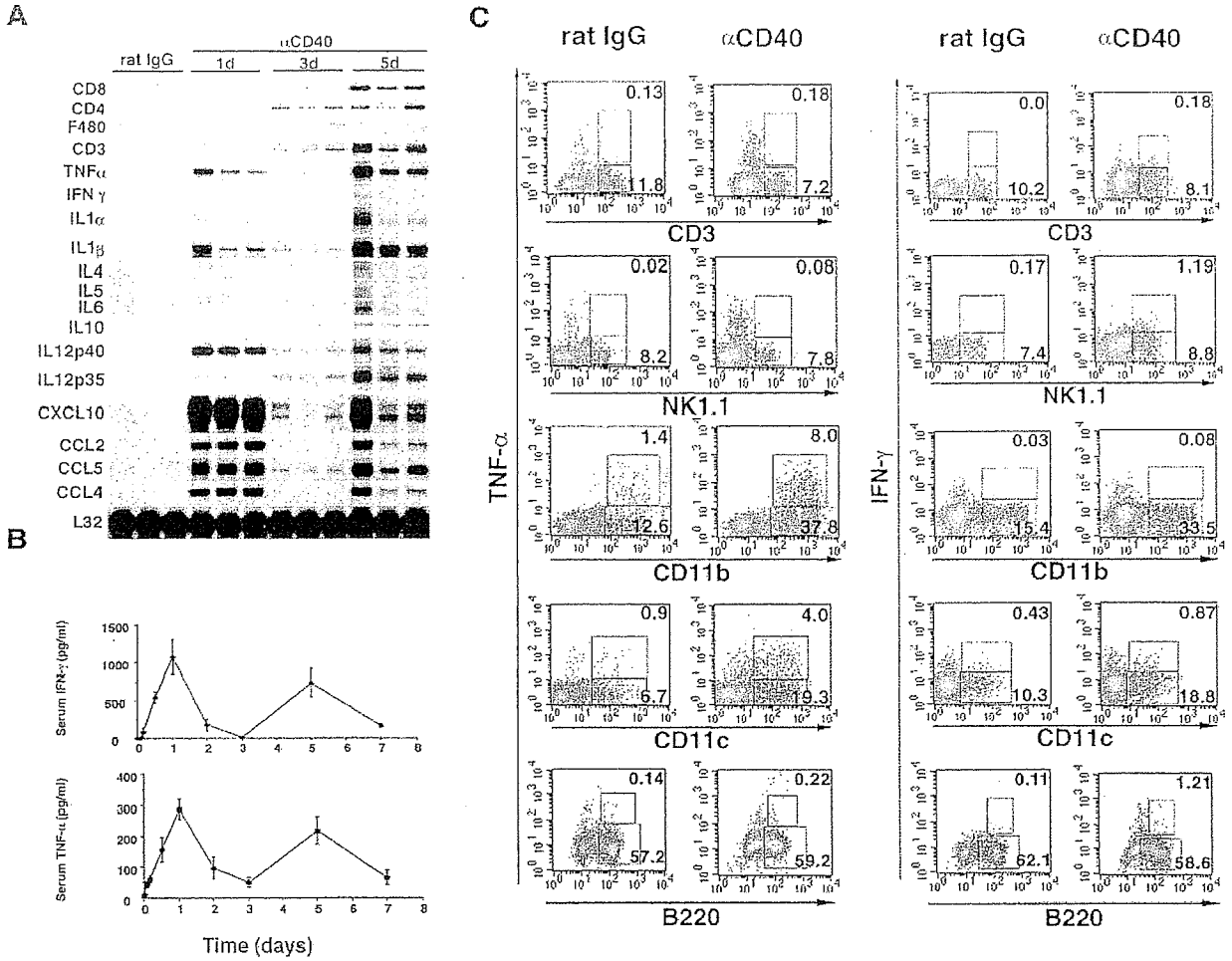


**Figure 2. A:** Injection of αCD40 causes liver injury. CB6F1 mice were injected intravenously with 100 μg of αCD40 and sacrificed at the indicated time points. Total hepatic RNA was analyzed for various cytokines and chemokines by RPA, as indicated. **B:** Serum IFN-γ and TNF-α concentrations. The serum IFN-γ and TNF-α concentrations were analyzed at the indicated time points after αCD40 injection in CB6F1 mice. The data are expressed as the mean ± SD. **C:** Intracellular cytokine expressions of IHLs. IHLs were stained with anti-mouse CD3, NK1.1, CD11b, CD11c, and B220-FITC, or anti-mouse IFN-γ and TNF-α-PE or APC, and analyzed using a FACScalibur system.

αCD40 injection. As shown in Figure 3A-1, αCD40 caused liver injury irrespective of the presence or absence of T cells, suggesting that intrahepatic $CD4^+$ and $CD8^+$ T cells did not contribute to the late-phase liver injury or affect the recruitment of NK cells, macrophages, dendritic cells, and B cells to the liver by αCD40 (Figure 3, A-2 and A-3). Consistent with the result of liver injury we found that depletion of T cells did not affect the cytokine and chemokine expression in the liver after injection (Figure 4A).

Next, to determine whether αCD40-induced late-phase liver injury requires NK cells, mice were treated with αasialo-GM1 antibody at days −1 and +2 relative to the αCD40 injection. We found that NK cell depletion also had little or no effect on total IHL recruitment (Figure 3, B-2 and B-3) or the severity of the liver disease (Figure 3B-1). Further, as shown in Figure 4B, we found that NK cell depletion significantly reduced IFN-γ, TNF-α, and CCL2 mRNA expression in the liver though CXCL10 and CCL5 mRNA expression revealed the similar levels. As we showed NK cells produced IFN-γ at this time point (Figure 2C), this result is consistent with the finding that NK cells can produce IFN-γ.

To evaluate the role of macrophages in this process, mice were treated with L-MDP, which induces apoptosis of macrophages in the liver *in vivo*.[23] One day later, the mice were injected intravenously with αCD40 or rat IgG. As shown in Figure 3C-1, elevation of sALT activity was significantly reduced in the L-MDP-treated mice, indicating that macrophages are necessary for liver injury on day 5 after αCD40 injection ($^*P < 0.05$). However, note that the sALT elevation was not completely blocked despite near total macrophage depletion (Figure 3C-1), suggesting that inflammatory cells other than macrophages may be involved in liver inflammation. Also note that a B-cell infiltrate was observed in the liver despite macrophage depletion, demonstrating that hepatic B-cell recruitment is primarily macrophage-independent.

Because the intrahepatic B-cell population increased massively after αCD40 injection, we investigated the role of B cells in the pathogenesis of the liver disease. μMT mice, which lack mature B cells because of a germline

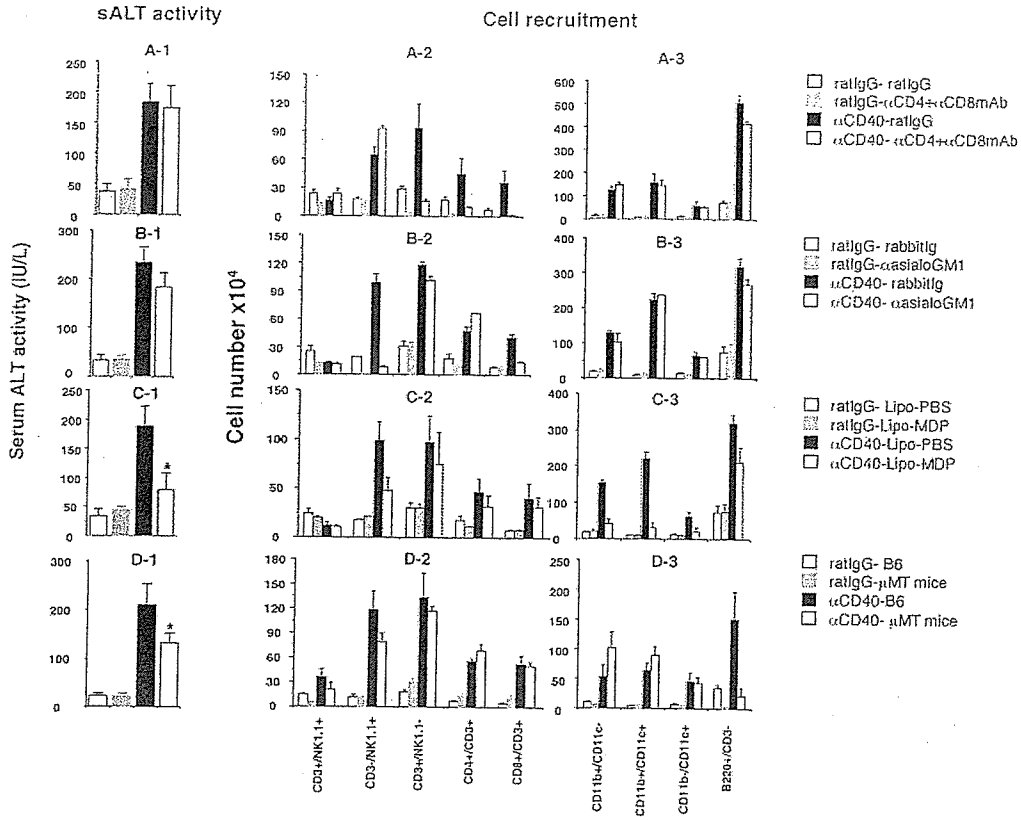


**Figure 3.** Depletion experiment. CB6F1 mice were injected with anti-mouse CD4 mAb (αCD4), anti-mouse CD8 mAb (αCD8), or control (rat IgG) antibodies at days −1 and +2 relative to the αCD40 injection and then sacrificed at day 5. The mean sALT activity expressed in IU/L is indicated for each group (**A-1**). IHLs from these animals were isolated and the absolute cell numbers were calculated (**A-2, A-3**). CB6F1 mice were injected with rabbit anti-mouse asialo-GM1 or control (rabbit Ig) antibodies at days −1 and +2 relative to the αCD40 injection and then sacrificed at day 5. sALT activity (**B-1**) and FACS (**B-2, B-3**) analyses were performed as described above. CB6F1 mice were injected with L-MDP or L-PBS at day −1 relative to the αCD40 injection and then sacrificed at day 5. sALT activity (**C-1**) and FACS (**C-2, C-3**) analyses were performed. μMT mice and C57BL/6 mice were injected with αCD40 or rat IgG and then sacrificed at day 5. sALT activity (**D-1**) and FACS (**D-2, D-3**) analyses were performed. All data are expressed as the mean ± SD for three mice. $^*P < 0.05$.

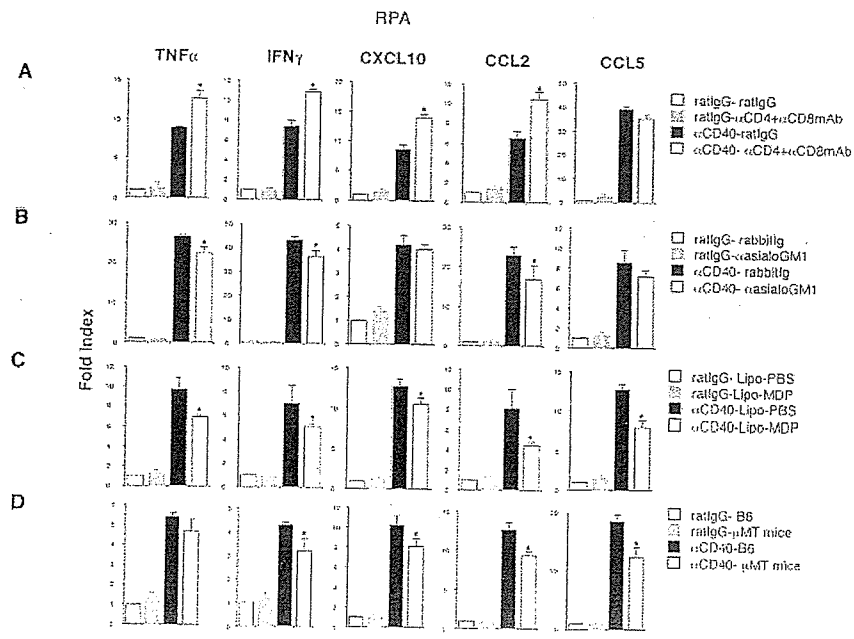


**Figure 4.** Cytokine and chemokine expression. Total hepatic RNA (20 μg) was isolated from the livers at various time points and analyzed for cytokine and chemokine expressions by RPA. To quantify the differences in the mRNA expressions at various groups, the mRNA expression levels were calculated as the relative percentage values of the L32 housekeeping gene expression. All data are expressed as the mean ± SD for three mice. $^*P < 0.05$.

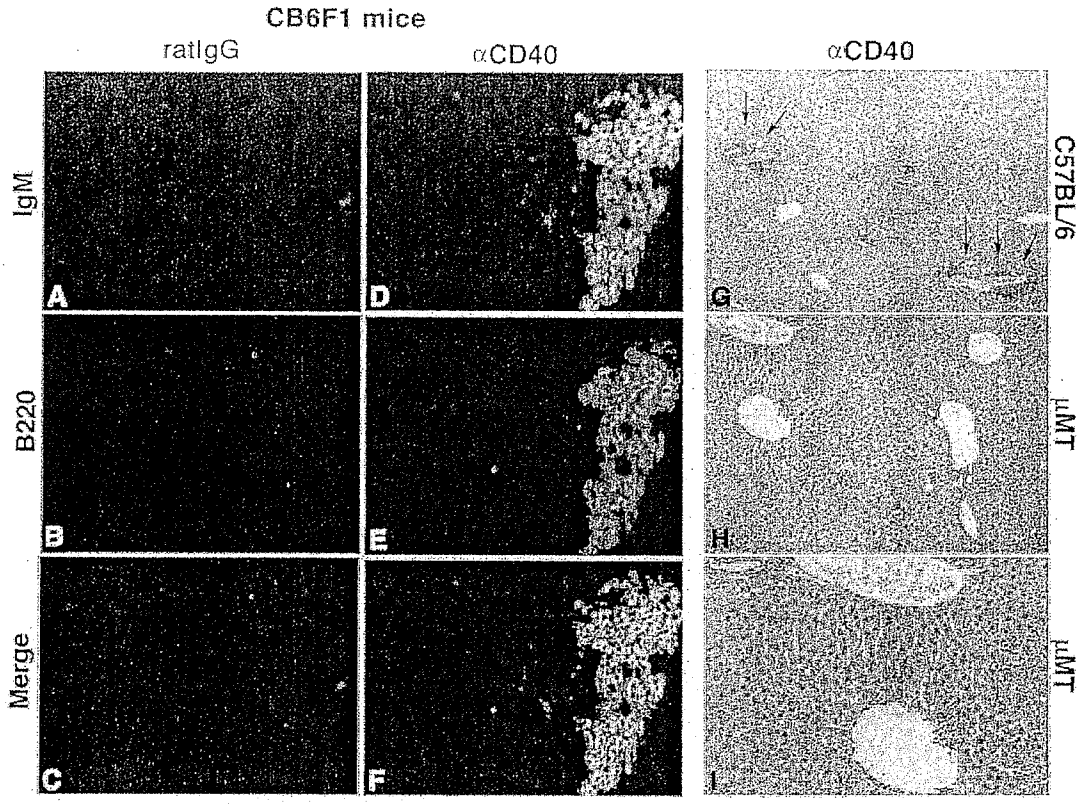


**Figure 5.** Histological analysis. Liver sections obtained from C57BL/6 mice sacrificed at day 5 after injection of αCD40 or rat IgG were stained with anti-mouse B220-PE and anti-mouse IgM-FITC antibodies (**A–F**). Liver sections were obtained from C57BL/6 or μMT mice sacrificed at day 5 after αCD40 injection and stained with H&E (**H–I**).

deletion of the membrane exon of the immunoglobulin μ heavy chain,[27] and C57BL/6 mice were treated with αCD40 or rat IgG, and sALT activity and IHL infiltration were monitored 5 days later. As shown in Figure 3D-1, μMT mice displayed less liver disease (sALT activity: 138 ± 18 U/L) than normal control mice (sALT activity: 212 ± 23 U/L) after αCD40 injection, and this difference was statistically significant ($^*P < 0.05$), suggesting that B cells contribute to the pathogenesis of αCD40-induced late-phase liver disease. Interestingly, macrophage and dendritic cell recruitment were increased in μMT mice (Figure 3, D-2 and D-3), perhaps accounting for the relatively modest reduction in the severity of liver disease in the B-cell knockout animals. In addition, importantly we found that IFN-γ, CXCL10, CCL2, and CCL5 mRNA expression reduced in the liver with μMT mice although TNF-α expression revealed the same level irrespective of B cell absence or presence (Figure 4D). These results suggested that B cells contribute to induction of IFN-γ and chemokines at late phase after αCD40 injection.

### *Histological Analysis*

To determine the distributions of B cells in the liver after αCD40 injection, we performed H&E staining and immunohistological staining. Histological analysis revealed that lymphocytes had infiltrated around the portal tract (Figure 5, arrow) and liver parenchyma with wild-type mice. In contrast, αCD40-treated μMT mice did not show infiltration of these cells around the portal tract (Figure 5, right). Immunohistochemical analysis revealed that huge numbers of $B220^+/IgM^+$ B cells had infiltrated into the parenchyma and around the portal tract and central vein on day 5 after the injection in wild-type mice (Figure 5, left).

### *Transfer of B Cells into SCID Mice*

To confirm the involvement of B cells in this model, we adoptively transferred $1 \times 10^7$ purified B cells isolated from the spleens of C.B.17 mice (Figure 6A) into SCID mice, and then injected αCD40 or rat IgG 1 day later. As shown in Figure 6A, sALT activity was significantly elevated in B-cell-reconstituted mice that received αCD40 compared with the NaCl-treated and rat IgG control groups ($^*P < 0.05$). Further, we also showed that total number of IHLs increased in B-cell-reconstituted mice as compared with NaCl-treated mice after αCD40 injection (Figure 6B). To evaluate which cell population is affected by adoptively transferred B cells, we analyzed the phenotype of IHLs by FACS. As shown in Figure 6B, we used anti-mouse CD49b/Pan-NK cells mAb (clone DX-5) instead of anti-mouse NK1.1 mAb (clone PK136) as a marker of NK cells in this experiment because the PK136 antibody does not stain NK cells in C.B.17 and SCID mice (data not shown).[28] Interestingly, the number of $CD3^-$/

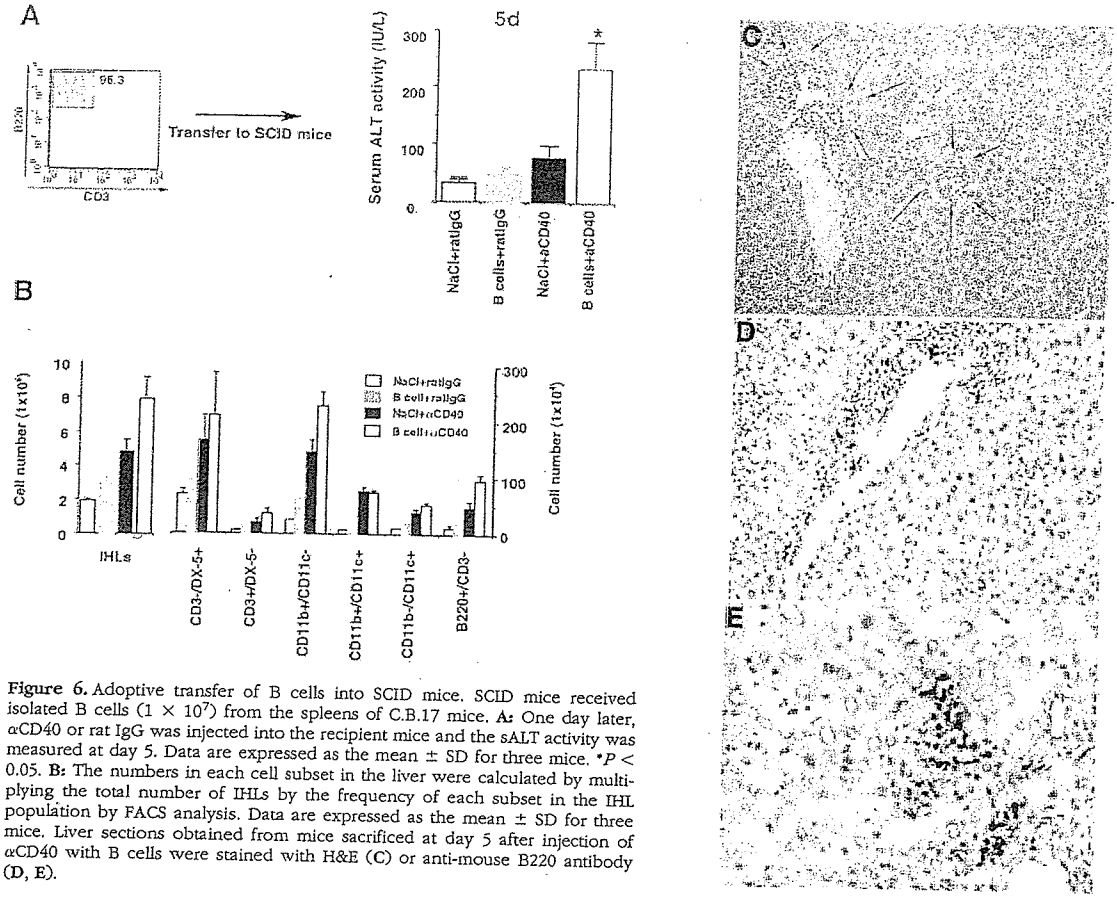


**Figure 6.** Adoptive transfer of B cells into SCID mice. SCID mice received isolated B cells ($1 \times 10^7$) from the spleens of C.B.17 mice. **A:** One day later, αCD40 or rat IgG was injected into the recipient mice and the sALT activity was measured at day 5. Data are expressed as the mean ± SD for three mice. $^*P < 0.05$. **B:** The numbers in each cell subset in the liver were calculated by multiplying the total number of IHLs by the frequency of each subset in the IHL population by FACS analysis. Data are expressed as the mean ± SD for three mice. Liver sections obtained from mice sacrificed at day 5 after injection of αCD40 with B cells were stained with H&E (**C**) or anti-mouse B220 antibody (**D, E**).

DX-5$^+$ cells (NK cells) and macrophages increased in B-cell-reconstituted mice, demonstrating that αCD40 activated B cells can induce the proliferation and recruitment of these inflammatory cells (Figure 6B). Consistent with the result of sALT activity, histological analysis revealed the presence of a necroinflammatory liver disease (Figure 6C, arrows) consisting of B cells that infiltrated the liver parenchyma (Figure 6, D and E). These results strongly support the hypothesis that B cells play a key role in αCD40-induced liver injury.

## *Determination of What Molecules Mediate αCD40-Induced Liver Injury*

First, to determine whether IFN-γ or TNF-α contribute to αCD40-induced late-phase liver injury, we injected CB6F1 mice with αIFN-γ or αTNF-α mAb, or an irrelevant hamster IgG before αCD40 administration. The αIFN-γ mAb completely blocked the induction of liver injury ($^*P < 0.05$) and greatly attenuated the intrahepatic inflammatory cell infiltrate (Figure 7, B and C) and cytokine/chemokine expression (Figure 7A and Supplemental Figure S1; for supplemental figure, see *http://ajp.amjpathol.org*) in the same animals, indicating that IFN-γ is primarily responsible for all these events.

In contrast, αTNF-α mAb treatment provided substantial but partial protection against late-phase liver injury (Figure 7B, left), which corresponded with its ability to only partially block the recruitment of NK and T cells into the liver (Figure 7B) and the induction of inflammatory cytokines and chemokines (Figure 7A). These results suggest that TNF-α also contributes to the pathogenetic activity of B cells and macrophages in the late phase of liver injury induced by αCD40.

Furthermore, to determine whether the Fas-Fas ligand pathway plays an important role in the liver injury, we injected αCD40 into Fas KO and C57BL/6 mice and then sacrificed them on day 5 for analysis. As shown in Figure 7D, we found that Fas KO mice displayed wild-type levels of serum ALT activity and inflammatory cell recruitment, indicating that the αCD40-induced liver disease is independent of the Fas pathway.

## *Discussion*

The results presented here demonstrate that CD40-activated B cells and macrophages can cause a necroinflammatory response in the liver by inducing inflammatory cytokines (especially IFN-γ and TNF-α) and chemokines that recruit additional inflammatory cells that damage the liver. We have previously shown that αCD40 causes a biphasic,

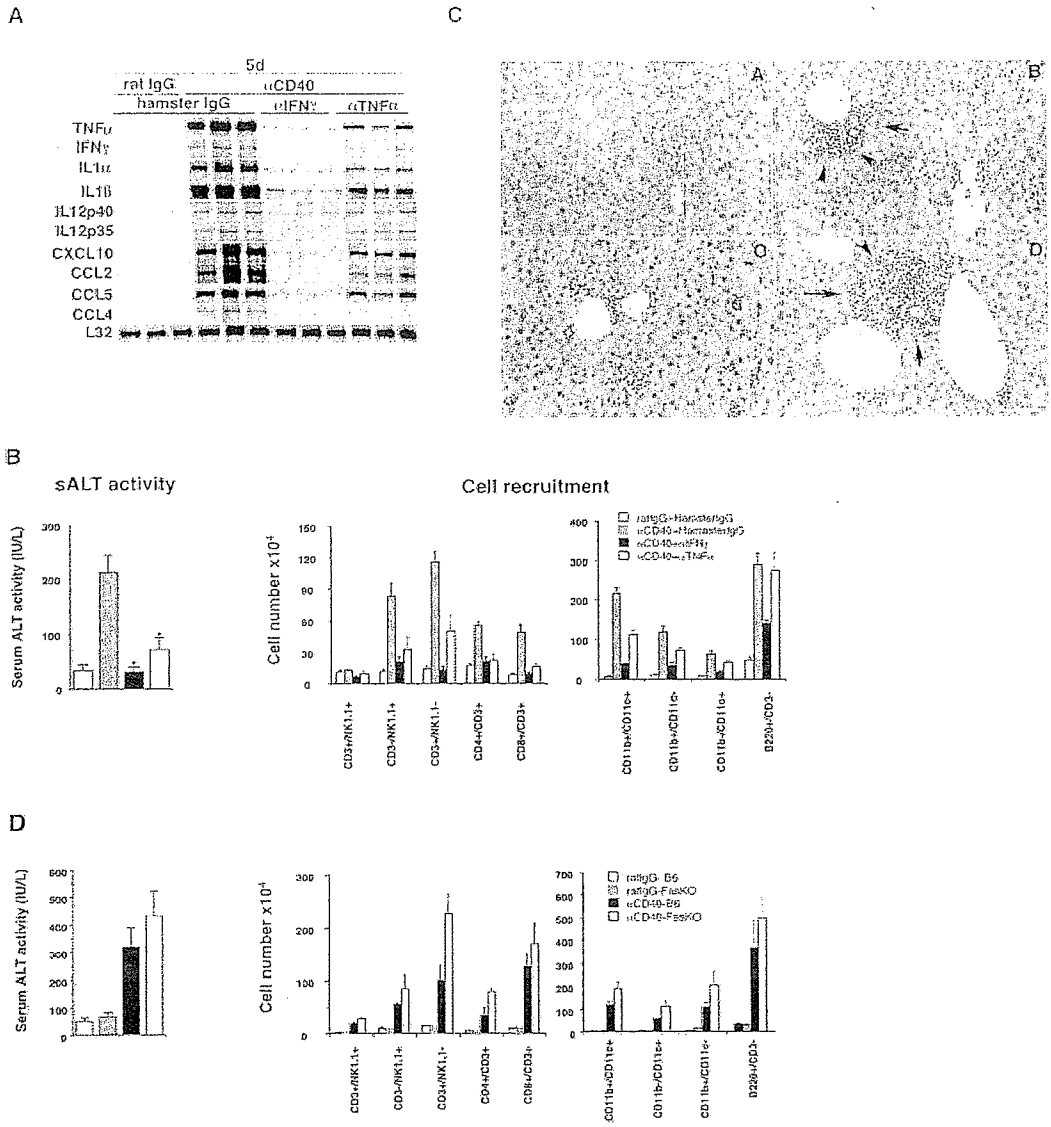


**Figure 7.** Liver injury induced by αCD40 is mediated by IFN-γ and TNF-α, but not by Fas. **A:** CB6F1 mice were injected with αIFN-γ or αTNF-α mAb, or control hamster IgG, before the injection of αCD40 or rat IgG. Total hepatic RNA was analyzed as described in the legend for Figure 2. The mean sALT activity expressed in IU/L is indicated for each group. **B:** IHLs from these animals were isolated and the effects of IFN-γ and TNF-α mAb, or a control antibody, on mice treated with αCD40 or rat IgG were analyzed. The numbers in each cell subset in the liver were calculated by multiplying the total number of IHLs by the frequency of each subset in the IHL population by FACS analysis. All data are expressed as the mean ± SD for three mice. $^*P < 0.05$. Histology. Liver sections obtained from mice sacrificed at day 5 after injection of rat IgG (**C-A**) or αCD40 with hamster IgG (**C-B**), αIFN-γ (**C-C**), or αTNF-α (**C-D**) were stained with H&E. **D:** The role of Fas. Fas KO and C57BL/6 mice were injected with αCD40 and then sacrificed at day 5. The mean sALT activity expressed in IU/L is indicated for each group. IHLs from these animals were isolated and the absolute cell numbers were calculated.

IFN-γ-, and TNF-α-dependent liver disease,[17] the first wave of which requires intrahepatic macrophages and NK cells. In the current study, we examined the pathophysiology of the second wave of the liver injury induced by CD40 ligation. Having observed that the liver injury occurred in the absence of macrophages, T cells, and NK cells after CD40 ligation while a large number of B cells infiltrated the portal and central veins in the liver during the delayed phase of the liver disease, we hypothesized that B cells might contribute to the pathogenesis of this disease.

On testing this hypothesis, we found that the late phase of αCD40-induced liver injury was suppressed in μMT mice and normal mice treated with L-MDP, but that depletion of T or NK cells had no effect. We confirmed the involvement of B cells in this model by showing that αCD40 treatment could cause liver injury after adoptive transfer of B cells into SCID mice (Figure 6). Based on these results, we conclude that αCD40-activated B cells and macrophages mediate the second wave of liver injury in this model. Although the potential of B cells to produce a variety of cytokines and chemokines is well demonstrated *in vitro*,[3,29] the ability of B cells to perform effector functions at inflammatory sites *in vivo* is not well defined. In the current article, we demonstrate that activated B cells can contribute to liver inflam-

mation. Nonetheless, several questions remain to be elucidated.

First, how do αCD40-activated B cells cause liver injury? One possible clue is our observation that αCD40 treatment causes liver injury and cell recruitment in Fas knockout mice as well as in wild-type mice (Figure 7). This result demonstrates that the liver disease is not Fas-Fas ligand-dependent, although CD40 ligation increases Fas expression in B cells.[11] Furthermore, we showed that the liver disease is mediated by inflammatory cytokines, especially IFN-γ and TNF-α. However, several points remain obscure. First, NK cell depletion by αasialo-GM1 treatment did not mitigate the liver disease or inflammatory cell recruitment, yet NK cells are the main producers of IFN-γ (Figure 2C). This suggests that cells other than NK cells, possibly B, T, and dendritic cells, produce the pathogenetic IFN-γ. Actually, we detected IFN-γ mRNA in the liver after αCD40 injection in NK cell-depleted mice (Figure 4) and also showed IFN-γ mRNA expression was suppressed in the liver with μMT mice (Figure 4). In support of this hypothesis, it has been reported that αCD40-activated B cells could produce IFN-γ and induce IFN-γ production on CD4 T cells.[3,30] Because IFN-γ is well known as a potent activator of macrophages,[31,32] and TNF-α (produced by macrophages) is also known to cause liver injury,[33] we hypothesize that αCD40 induced B cell and secondary activated other inflammatory cell-derived IFN-γ may be the inducer in the cascade leading to liver inflammation, and that IFN-γ activates macrophages and other inflammatory cells that serve as effectors in this disease. This scenario is supported by the findings that IFN-γ blockade completely protects against αCD40-induced liver injury and cell recruitment, whereas TNF-α blockade confers only partial protection. Importantly, as shown in Figure 3, we found that αCD40 treatment induced the migration of macrophages, dendritic cells, and NK cells in μMT mice, indicating that these cells can be recruited into the liver without B cell help, and suggesting that they also contribute to the residual late phase in the B-cell knockout animals.

Furthermore, we found that liver injury was observed in μMT mice and reduced in L-MDP-treated mice, indicating that macrophages also contribute to liver inflammation in this model. Notably, we confirmed that αCD40-induced liver injury was completely prevented by depletion of both B cells and macrophages in the liver (Supplemental Figure S2 at *http://ajp.amjpathol.org*). It is well known that macrophages can induce liver injury through cytokine production.[34–36] Accordingly, the interaction of macrophages and B cells in this liver injury model is interesting. We found that co-culture of B cells and macrophages under αCD40 treatment increased IFN-γ or TNF-α production, respectively, as compared with single cells (data not shown). These findings suggested that B cells and macrophages could stimulate each other by cell-to-cell or cytokine under some conditions. However, we have shown here that B cells infiltrate the liver in macrophage-depleted animals after CD40 ligation. In contrast, macrophages were also recruited to the liver in μMT mice after stimulation (Figure 3). Consistent with the fact that CD40 ligation induces macrophage and B cell activation and proliferation independently[11,37,38] we consider that these cells work to establish liver inflammation independently in this system.

Interestingly, despite showing that B cells play an important role in the late-phase liver injury, we demonstrated that B cells do not contribute to the early phase liver disease (Supplemental Figure S3 at *http://ajp.amjpathol.org*). Furthermore, we found that the increase of intrahepatic B cells was small on day 1 after αCD40 injection, indicating that recruitment and proliferation in B cells was not enough to function as effector cells at this time. With regard to effector functions of B cells, we have to exclude the possibility that CD40 ligation induced antibody-dependent effector functions because CD40 ligation can induce autoreactive antibody.[12,39,40] To evaluate this hypothesis, we examined the number of antibody-producing cells, plasma cell populations in IHLs and spleen after αCD40 injection. As shown in Supplemental Figure S4 at *http://ajp.amjpathol.org*, we found antibody-secreting cells ($B220^+/CD138^+$) in IHLs and spleen peaked at day 3 after injection despite liver injury were not observed at this time, suggesting that antibody-dependent mechanisms are not responsible for liver injury in this model.

Recently antibody-independent contributions of B cells have been demonstrated in murine models of autoimmune disease. Chan and colleagues[41] have shown that MLR/lpr mice that are deficient in their ability to secrete Ig develop interstitial nephritis, vasculitis, and mortality when compared with secretary sufficient MLR/lpr. Based on this precedent, we suggest that CD40-activated B cells behave as effector cells in an antibody-independent manner in the current model.

Finally, we have also an interest for the role of NKT cells in this liver inflammation because NKT cells are abundant in the liver and recovered to base line at the late phase after αCD40 injection (data not shown). A current report shows NKT cells recognize an endogenous ligand presented by CD1d on B cells and regulate B-cell proliferation and effector functions.[42] This result suggests that NKT cells also might activate B cells and accelerate liver injury in this model.

In summary, we have shown here that αCD40-activated B cells and macrophages produce inflammatory cytokines and contribute to the pathogenesis of a necroinflammatory liver disease. The present data illustrate that activated B cells can both cause and amplify tissue injury, and provide new evidence that B cells can function in a pathogenic manner at sites of tissue inflammation.

## *Acknowledgments*

We thank Dr. Antonius Rolink (Basel Institute for Immunology) for providing the anti-mouse agonistic CD40 monoclonal antibody, Dr. Rolf Zinkernagel (University of Zurich) for providing the anti-mouse CD4 and CD8 antibodies, Dr. Robert Schreiber (Washington University) for providing the anti-mouse IFN-γ and TNF-α antibodies, Dr. Shigekazu Nagata (Osaka University) for providing the Fas KO mice, and Dr. Kazuhiro Kakimi (Tokyo Medical University School of Medicine) for critical advice.

## References


1. Bachmann MF, Zinkernagel RM: Neutralizing antiviral B cell responses. Annu Rev Immunol 1997, 15:235–270
2. Schaniel C, Pardali E, Sallusto F, Speletas M, Ruedl C, Shimizu T, Seidl T, Andersson J, Melchers F, Rolink AG, Sideras P: Activated murine B lymphocytes and dendritic cells produce a novel CC chemokine which acts selectively on activated T cells. J Exp Med 1998, 188:451–463
3. Harris DP, Haynes L, Sayles PC, Duso DK, Eaton SM, Lepak NM, Johnson LL, Swain SL, Lund FE: Reciprocal regulation of polarized cytokine production by effector B and T cells. Nat Immunol 2000, 1:475–482
4. Maccioni M, Zeder-Lutz G, Huang H, Ebel C, Gerber P, Hergueux J, Marchal P, Duchatelle V, Degott C, van Regenmortel M, Benoist C, Mathis D: Arthritogenic monoclonal antibodies from K/BxN mice. J Exp Med 2002, 195:1071–1077
5. Ji H, Ohmura K, Mahmood U, Lee DM, Hofhuis FM, Boackle SA, Takahashi K, Holers VM, Walport M, Gerard C, Ezekowitz A, Carroll MC, Brenner M, Weissleder R, Verbeek JS, Duchatelle V, Degott C, Benoist C, Mathis D: Arthritis critically dependent on innate immune system players. Immunity 2002, 16:157–168
6. Fillatreau S, Sweenie CH, McGeachy MJ, Gray D, Anderton SM: B cells regulate autoimmunity by provision of IL-10. Nat Immunol 2002, 3:944–950
7. Donaldson P, Doherty D, Underhill J, Williams R: The molecular genetics of autoimmune liver disease. Hepatology 1994, 20:225–239
8. Peters M, Vierling J, Gershwin ME, Milich D, Chisari FV, Hoofnagle JH: Immunology and the liver. Hepatology 1991, 13:977–994
9. Grewal IS, Flavell RA: CD40 and CD154 in cell-mediated immunity. Annu Rev Immunol 1998, 16:111–135
10. Grewal IS, Borrow P, Pamer EG, Oldstone MB, Flavell RA: The CD40-CD154 system in anti-infective host defense. Curr Opin Immunol 1997, 9:491–497
11. Banchereau J, Bazan F, Blanchard D, Briere F, Galizzi JP, van Kooten C, Liu YJ, Rousset F, Saeland S: The CD40 antigen and its ligand. Annu Rev Immunol 1994, 12:881–922
12. Grewal IS, Flavell RA: A central role of CD40 ligand in the regulation of CD4+ T-cell responses. Immunol Today 1996, 17:410–414
13. Dullforce P, Sutton DC, Heath AW: Enhancement of T cell-independent immune responses in vivo by CD40 antibodies. Nat Med 1998, 4:88–91
14. Turner JG, Rakhmilevich AL, Burdelya L, Neal Z, Imboden M, Sondel PM, Yu H: Anti-CD40 antibody induces antitumor and antimetastatic effects: the role of NK cells. J Immunol 2001, 166:89–94
15. Wiley JA, Geha R, Harmsen AG: Exogenous CD40 ligand induces a pulmonary inflammation response. J Immunol 1997, 158:2932–2938
16. Wiley JA, Harmsen AG: Bone marrow-derived cells are required for the induction of a pulmonary inflammatory response mediated by CD40 ligation. Am J Pathol 1999, 154:919–926
17. Kimura K, Kakimi K, Wieland S, Guidotti LG, Chisari FV: Activated intrahepatic antigen-presenting cells inhibit hepatitis B virus replication in the liver of transgenic mice. J Immunol 2002, 169:5188–5195
18. Kimura K, Nagaki M, Takai S, Satake S, Moriwaki H: Pivotal role of nuclear factor κB signaling in anti-CD40-induced liver injury in mice. Hepatology 2004, 40:1180–1189
19. Adachi M, Suematsu S, Kondo T, Ogasawara J, Tanaka T, Yoshida N, Nagata S: Targeted mutation in the Fas gene causes hyperplasia in peripheral lymphoid organs and liver. Nat Genet 1995, 11:294–300
20. Schreiber RD, Hicks LJ, Celada A, Buchmeier NA, Gray PW: Monoclonal antibodies to murine gamma-interferon which differentially modulate macrophage activation and antiviral activity. J Immunol 1985, 134:1609–1618
21. Sheehan KC, Ruddle NH, Schreiber RD: Generation and characterization of hamster monoclonal antibodies that neutralize murine tumor necrosis factors. J Immunol 1989, 142:3884–3893
22. Cobbold SP, Martin G, Qin S, Waldmann H: Monoclonal antibodies to promote marrow engraftment and tissue graft tolerance. Nature 1986, 323:164–166
23. Naito M, Nagai H, Kawano S, Umezu H, Zhu H, Moriyama H, Yamamoto T, Takatsuka H, Takei Y: Liposome-encapsulated dichloromethylene diphosphonate induces macrophage apoptosis in vivo and in vitro. J Leukoc Biol 1996, 60:337–344
24. Leenen PJ, de Bruijn MF, Voerman JS, Campbell PA, van Ewijk W: Markers of mouse macrophage development detected by monoclonal antibodies. J Immunol Methods 1994, 174:5–19
25. Ezekowitz RA, Gordon S: Down-regulation of mannosyl receptor-mediated endocytosis and antigen F4/80 in bacillus Calmette-Guerin-activated mouse macrophages. Role of T lymphocytes and lymphokines. J Exp Med 1982, 155:1623–1637
26. Austyn JM, Gordon S: F4/80, a monoclonal antibody directed specifically against the mouse macrophage. Eur J Immunol 1981, 11:805–815
27. Kitamura D, Roes J, Kuhn R, Rajewsky K: A B cell-deficient mouse by targeted disruption of the membrane exon of the immunoglobulin mu chain gene. Nature 1991, 350:423–426
28. Yokoyama WM, Seaman WE: The Ly-49 and NKR-P1 gene families encoding lectin-like receptors on natural killer cells: the NK gene complex. Annu Rev Immunol 1993, 11:613–635
29. Pistoia V: Production of cytokines by human B cells in health and disease. Immunol Today 1997, 18:343–350
30. Duddy ME, Alter A, Bar-Or A: Distinct profiles of human B cell effector cytokines: a role in immune regulation? J Immunol 2004, 172:3422–3427
31. Nakanishi K, Yoshimoto T, Tsutsui H, Okamura H: Interleukin-18 regulates both Th1 and Th2 responses. Annu Rev Immunol 2001, 19:423–474
32. Guidotti LG, Chisari FV: Noncytolytic control of viral infections by the innate and adaptive immune response. Annu Rev Immunol 2001, 19:65–91
33. Bradham CA, Plumpe J, Manns MP, Brenner DA, Trautwein C: Mechanisms of hepatic toxicity. I. TNF-induced liver injury. Am J Physiol 1998, 275:G387–G392
34. Canbay A, Feldstein AE, Higuchi H, Werneburg N, Grambihler A, Bronk SF, Gores GJ: Kupffer cell engulfment of apoptotic bodies stimulates death ligand and cytokine expression. Hepatology 2003, 38:1188–1198
35. Dambach DM, Watson LM, Gray KR, Durham SK, Laskin DL: Role of CCR2 in macrophage migration into the liver during acetaminophen-induced hepatotoxicity in the mouse. Hepatology 2002, 35:1093–1103
36. Wolf D, Schumann J, Koerber K, Kiemer AK, Vollmar AM, Sass G, Papadopoulos T, Bang R, Klein SD, Brune B, Tiegs G: Low-molecular-weight hyaluronic acid induces nuclear factor-κB-dependent resistance against tumor necrosis factor α-mediated liver injury in mice. Hepatology 2001, 34:535–547
37. van Kooten C, Banchereau J: CD40-CD40 ligand. J Leukoc Biol 2000, 67:2–17
38. Calderhead DM, Kosaka Y, Manning EM, Noelle RJ: CD40-CD154 interactions in B-cell signaling. Curr Top Microbiol Immunol 2000, 245:73–99
39. Kaneko Y, Hirose S, Abe M, Yagita H, Okumura K, Shirai T: CD40-mediated stimulation of B1 and B2 cells: implication in autoantibody production in murine lupus. Eur J Immunol 1996, 26:3061–3065
40. Hirose S, Yan K, Abe M, Jiang Y, Hamano Y, Tsurui H, Shirai T: Precursor B cells for autoantibody production in genomically Fas-intact autoimmune disease are not subject to Fas-mediated immune elimination. Proc Natl Acad Sci USA 1997, 94:9291–9295
41. Chan OT, Hannum LG, Haberman AM, Madaio MP, Shlomchik MJ: A novel mouse with B cells but lacking serum antibody reveals an antibody-independent role for B cells in murine lupus. J Exp Med 1999, 189:1639–1648
42. Galli G, Nuti S, Tavarini S, Galli-Stampino L, De Lalla C, Casorati G, Dellabona P, Abrignani S: CD1d-restricted help to B cells by human invariant natural killer T lymphocytes. J Exp Med 2003, 197: 1051–1057

J Inherit Metab Dis (2006) 29:755–761
DOI 10.1007/s10545-006-0440-7

ORIGINAL ARTICLE

# Effect of Hunter disease (mucopolysaccharidosis type II) mutations on molecular phenotypes of iduronate-2-sulfatase: Enzymatic activity, protein processing and structural analysis

**K. Sukegawa-Hayasaka · Z. Kato · H. Nakamura · S. Tomatsu · T. Fukao · K. Kuwata · T. Orii · N. Kondo**

Received: 28 July 2006 / Submitted in revised form: 18 September 2006 / Accepted: 19 September 2006 / Published online: 7 November 2006


**Summary** Mucopolysaccharidosis II (Hunter disease), a lysosomal storage disorder caused by a deficiency of iduronate-2-sulfatase (IDS), has variable clinical phenotypes. Nearly 300 different mutations have been identified in the IDS gene from patients with Hunter disease, but the correlation between the genotype and phenotype has remained unclear. We studied the characteristics of 11 missense mutations, which were detected in the patients or artificially introduced, using stable expression experiments and structural analysis. The mutants found in the attenuated phenotype showed considerable residual activity (0.2–2.4% of the wild-type IDS activity) and those in the severe phenotype had no activity. In immunoblot analysis, both the 73–75 kDa precursor and processed forms were detected in the expression of 'attenuated' mutants (R48P, A85T and W337R) and the artificial active site mutants (C84S, C84T). The 73–75 kDa initial precursor was detected in the 'severe' mutants (P86L, S333L, S349I, R468Q, R468L). The truncated 68 kDa precursor form was synthesized in the Q531X mutant. The results of immunoblotting indicated rapid degradation and/or insufficiency in processing as a result of structural alteration of the IDS protein. A combination of analyses of genotype and molecular phenotypes, including enzyme activity, protein processing and structural analysis with an engineered reference protein, could provide an avenue to understanding the molecular mechanism of the disease and could give a useful tool for the evaluation of possible therapeutic chemical compounds.

Communicating editor: Ed Wraith

Competing interests: None declared

References to electronic databases: Iduronate-2-sulfatase EC3.1.6.13; mucopolysaccharidoisis II (Hunter disease) OMIM 309900

K. Sukegawa-Hayasaka (✉) · T. Fukao
Department of Pediatrics, Gifu University Graduate School of Medicine, Gifu, Japan
e-mail: k-hayasaka@m6.dion.ne.jp

Z. Kato
Department of Pediatrics, Gifu University Graduate School of Medicine, Gifu, Japan; Division of Virology, Center for Emerging Infectious Diseases (CEID), Gifu University, Gifu, Japan; Center for Advanced Drug Research (CADR), Gifu University, Gifu, Japan; Molecular and Cellular Biology, Harvard University, Cambridge, Massachusetts, USA

N. Kondo
Department of Pediatrics, Gifu University Graduate School of Medicine, Gifu, Japan; Division of Virology, Center for Emerging Infectious Diseases (CEID), Gifu University, Gifu, Japan; Center for Advanced Drug Research (CADR), Gifu University, Gifu, Japan

H. Nakamura
Research Center for Structural Biology, Institute for Protein Research, Osaka University, Osaka, Japan

S. Tomatsu
Department of Pediatrics, Gifu University Graduate School of Medicine, Gifu, Japan; Department of Pediatrics, St. Louis University, Pediatric Research Institute, St. Louis, Missouri, USA

K. Kuwata
Division of Prion Research, Center for Emerging Infectious Diseases (CEID), Gifu University, Gifu, Japan

T. Orii
Department of Human Welfare, Faculty of Human Welfare, Chubu Gakuin University, Gifu, Japan

## Abbreviations

| | |
|---|---|
| IDS | iduronate-2-sulfatase |
| 4S | arylsulfatase B (*N*-acetylgalactosamine-4S sulfatase) |
| ASA | arylsulfatase A |
| GALNS | *N*-acetylgalactosamine-6S sulfatase |

## Introduction

Mucopolysaccharidosis II (Hunter disease) is an X-linked recessive disorder caused by a deficiency of iduronate-2-sulfatase (IDS; EC 3.1.6.13, OMIM 309900). The enzyme deficiency leads to the accumulation of heparan sulfate and dermatan sulfate in lysosomes and higher excretion of them in the urine. Clinically, a wide spectrum of phenotypes has been observed, ranging from severe to attenuated. The severe form is characterized by progressive clinical deterioration with mental retardation, multiple skeletal deformities and organ and soft-tissue involvement that leads to death, often before 15 years of age. In contrast, the attenuated form is characterized by joint stiffness and relatively mild somatic changes without mental retardation. Although the patients with the attenuated form present with a wide range of severities, they may survive into adulthood (Neufeld and Muenzer 2001). IDS cDNA and its genomic DNA gene have been isolated and characterized (Flomen et al 1993; Robert et al 1989; Wilson et al 1990, 1993). Nearly 300 different mutations have been described in Hunter patients (http://www.hgmd.org/); some of the mutations have been examined in expression studies (Bonuccelli et al 2001; Chang et al 2005; Crotty et al 1992; Cudry et al 2000; Millat et al 1997, 1998; Ricci et al 2003; Sukegawa et al 1995; Villani et al 2000), but the correlation between genotype and phenotype has remained unclear. We previously identified the missense and nonsense mutations of the IDS gene in Hunter disease and characterized the mutant proteins with the transiently transfected cells (Sukegawa et al 1992, 1995). However, we observed little residual enzyme activity in the mutant proteins. It is likely that the residual enzyme activities expressed by the mutant cDNAs were be too low to allow for biochemical characterization in the transient expression assay.

In this study, we characterized 11 mutant iduronate-2-sulfatase proteins that were stably expressed in CHO cells, and of which the C84S and S349I mutations have not previously been studied by expression analysis. We discuss the effect of the mutations on the molecular phenotypes, including enzyme activity, protein processing and structural features using engineered reference proteins.

## Methods and materials

### Mutations of the IDS gene in Hunter patients

In earlier work we identified the missense and nonsense mutations of the IDS gene in Hunter disease (Isogai et al 1998) and characterized the mutant proteins with the transiently transfected cells (Sukegawa et al 1992, 1995). In the present study, we focused on the common mutations and analysed nine mutations and two artificial active site mutations. P86L, S333L, S349I, R468Q and R468L were 'severe' mutations. R48P, A85T, W337R and Q531X were 'attenuated' mutations. C84S and C84T were the predictive active site mutations.

Informed consent was obtained from the patients to perform the enzyme assay and molecular analysis. This study was approved by the review board of Gifu University School of Medicine.

### Expression of the IDS wild-type and IDS mutants in CHO cells

The wild-type IDS cDNA (Sukegawa et al 1995) was subcloned into pUC13. Site-directed mutagenesis was performed using a QuickChange site-directed mutagenesis kit (Stratagene, La Jolla, CA, USA) according to the supplier's protocol. The wild-type and mutant cDNAs were excised from the pUC13 vector with *Eco*RI and introduced into the expression vector, pCXN2. All final constructs were verified by semi-automated sequencing. The CHO cells were grown in Ham's F12 medium containing 10% fetal calf serum. The wild-type and mutant pCXN2-IDS were transfected into CHO cells by electroporation. The experimental conditions were: $4 \times 10^6$ cells, 20 μg of plasmid DNA and a voltage pulse of 1200 V, 25 μF. After electroporation, the cells were seeded on 10 cm plates. At 48 h post electroporation, the cells were selected with G418. The colonies were picked up and were cultured in the above medium. The cells were harvested and kept at −80°C until use. The cell homogenate was prepared by sonication in extraction buffer (20 mmol/L Tris-HCl pH7.5, 50 μmol/L phenylmethylsulfonyl fluoride) at 4°C, and was used for the enzyme assays of IDS activity and western blot analysis as described below.

### IDS enzyme assay

IDS activity was measured by the procedure of Hall and colleagues (1978) using the radiolabelled disaccharide as the substrate. The total protein concentration was measured according to the method of Lowry et al (1951).

### Western blot analysis

Western blotting was performed as previously described (Sukegawa et al 2000), using 20 μg protein of the total cell extract from transfected CHO cells. The human IDS monoclonal antibody was used to detect the proteins (Sukegawa et al 1992).

Construction of a tertiary model for IDS protein

A tertiary model of the human IDS protein was constructed by homology modelling using our original programs: a loop search method for the backbone structure (Nakamura et al 1991), a dead-end elimination method for side-chain conformation (Tanimura et al 1994), and conformation energy minimization for structure refinement (Morikami et al 1992), using the AMBER force field (Weiner et al 1986). Human arylsulfatase B (Bond et al 1997) and human arylsulfatase A (Lukatela et al 1998) were used as templates for the construction of the model.

## Results and discussion

In the present study, we reproduced nine of the identified mutations and two artificial active site mutations in order to evaluate the functional consequences on IDS activity and processing, and the structural model was constructed to discuss the results.

Enzymatic activity of IDS

The total IDS activity of cell homogenates from the wild-type construct showed a significant increase of the enzymatic activity with excellent reproducibility (Table 1). The total IDS activity of cell homogenates from all the mutants showed significant decreases but with different magnitudes (Table 1). The P86L, S333L, S349I, R468Q and R468L mutants, which were found in the patients with the severe phenotype, had a very low activity that was below the resolution limit of the IDS assay or had no activity. The R48P, A85T, W337R and Q531X mutants had residual activity (0.2–2.4% of the wild-type IDS activity) and all were present in the patients with the attenuated phenotype. In addition, C84S and C84T, engineered as predictive active site mutations (Schmidt et al 1995), had no activity. Thus, significant residual activity was found in mutants from the attenuated patients, and this finding served as a guide to prediction of the molecular phenotype of the mutants.

Protein processing

IDS processing has been reported (Froissart et al 1995). The 75–78 kDa initial precursor is synthesized and converted into the phosphorylated 90 kDa form. The 90 kDa precursor is then processed by the glycosylation modifications and proteolytic cleavages through various intermediates to the 55 kDa and 45 kDa mature forms. We analysed the mutant IDS proteins by western blotting (Fig. 1). The 73–75 kDa precursor, and 55–56 kDa and 44–45 kDa mature polypeptides were observed in the cell homogenates from the wild-type, A85T mutant, and C84S and C84T of the predictive active site mutants. In the R48P and W337R mutants, which were found in the patients with the attenuated phenotype, the 73–75 kDa precursor was synthesized and processed to intermediate forms but mature forms were not detected. The truncated 68 kDa precursor form was synthesized in the Q531X mutant. In the P86L, S333L, S349I, R468Q and R468L mutants, which were found in the patients with the severe phenotype, the 73–75 kDa initial precursor was detected. The results of western blotting showed only the primary immature precursors without any mature forms, indicating a rapid degradation and/or an insufficiency in processing as a result of structural alteration of the IDS protein.

**Table 1** Iduronate 2-sulfatase activities in stably transfected CHO cells

| Mutation | Clinical phenotypes of patients | IDS activity (nmol/h per mg) | Patients in reference[a] |
|---|---|---|---|
| Untransfected | | n.d. ($n=4$) | |
| Wild | Normal | $1529 \pm 327$ ($n=7$) | |
| R48P | Attenuated | $5 \pm 3$ ($n=5$) | HT2 |
| A85T | Attenuated | $19 \pm 7$ ($n=5$) | HT65 |
| W337R | Attenuated | $3 \pm 1$ ($n=5$) | HT4 |
| Q531X | Attenuated | $36 \pm 12$ ($n=5$) | HT5 |
| P86L | Severe | n.d. ($n=4$) | HT10 |
| S333L | Severe | n.d. ($n=4$) | HT11 |
| S349I | Severe | n.d. ($n=4$) | HT39 |
| R468Q | Severe | n.d. ($n=4$) | HT40 |
| R468L | Severe | n.d. ($n=4$) | HT13, 38, 61 |
| C84S | Artificial mutation | n.d. ($n=4$) | |
| C84T | Artificial mutation | n.d. ($n=4$) | |

IDS activity values are the average of the different clones.
$n$, number of the different clones of untransfected or transfected cells.
[a]Isogai et al (1998).